

C O M M U N I C A T I O N S

FACULTY OF SCIENCES
UNIVERSITY OF ANKARA

DE LA FACULTE DES SCIENCES
DE L'UNIVERSITE D'ANKARA

Series A2-A3: Physical Sciences and Engineering

VOLUME: 62

Number: 2

YEAR: 2020

Faculty of Sciences, Ankara University
06100 Beşevler, Ankara-Turkey
ISSN 1303-6009 E-ISSN 2618-6462

C O M M U N I C A T I O N S

FACULTY OF SCIENCES
UNIVERSITY OF ANKARA

DE LA FACULTE DES SCIENCES
DE L'UNIVERSITE D'ANKARA

Series A2-A3: Physical Sciences and Engineering

Volume 62

Number : 2

Year :2020

Owner

Sait HALICIOĞLU, Dean of Faculty of Sciences

Editor in Chief

Nuri ÖZALP

Managing Editor

A. Ulvi YILMAZER

Area Editors

Ali YAMAN (Physics)

Iman ASKERZADE(Askerbeyli)(Computer Eng.)

Tülay SERİN (Engineering Physics)

Ziya TELATAR(Electronic Engineering)

H. Volkan ŞENAVCI (Astronomy)

M. Emin CANDANSAYAR (Geophysical Eng.)

Editors

Ramiz ALIGULIYEV

Azerbaijan National Academy of Sciences

Osman EROGLU

TOBB Economy and Tech. Uni., TURKEY

Ilhan KOSALAY

Ankara University, TURKEY

Miroslav VOZNAK

VŠB – Tech.Uni. of Ostrava, CZECH REPUBLIC

Roy L. STREIT

Uni. of Massachusetts at Dartmouth, USA

Gabriela CIUPRINA

Politehnica Uni. of Bucharest, ROMANIA

H. Gokhan ILK

Ankara University, TURKEY

Isa NAVRUZ

Ankara University, TURKEY

Emre YENGEL

King Abdullah Uni. of Sci. and Tech. (KAUST),

SAUDI ARABIA

Kutluay YUCE

Ankara University, TURKEY

Murat EFE

Ankara University, TURKEY

Mustafa E. KAMASAK

Istanbul Tech. Uni., TURKEY

Hakan TORA

Atilim University, TURKEY

A. Egemen YILMAZ

Ankara University, TURKEY

This Journal is published two issues in a year by the Faculty of Sciences, University of Ankara. Articles and any other material published in this journal represent the opinions of the author(s) and should not be construed to reflect the opinions of the Editor(s) and the Publisher(s).

Correspondence Address:

COMMUNICATIONS

EDITORIAL OFFICE

Ankara University, Faculty of Sciences,

06100 Tandoğan, ANKARA – TURKEY

Tel: (90) 312-212 67 20 Fax: (90) 312-223 23 95

e-mail: commun@science.ankara.edu.tr

<http://communications.science.ankara.edu.tr/index.php?series=A2A3>

Print:

Ankara University Press

İncitaş Sokak No:10 06510 Beşevler

ANKARA – TURKEY

C O M M U N I C A T I O N S

FACULTY OF SCIENCES
UNIVERSITY OF ANKARA

DE LA FACULTE DES SCIENCES
DE L'UNIVERSITE D'ANKARA

Series A2-A3: Physical Sciences and Engineering

Volume 62

Number : 2

Year :2020

L. ÖZBEK, L. SÜTÇİGİL, H. AYDIN, S. YETKİN, F. ÖZGEN, A statistical overview on sleep scoring	115
K. CENGİZ, Analyzing the performance of pure lateration in indoor environments with various performance metrics	123
A. BEKTAŞ, H. ERGEZER, LPI radar waveform classification using binary SVM and multi-class SVM based on principal components of TFI	134
M. ÜNAL, E. BOSTANCI, M.S. GUZEL, A. AYDIN, Modern learning techniques and plant image classification	153
İ. NAVRUZ, M.BİLSEL, A concatenated up and down tapered fiber for simultaneous measurement of strain and temperature..	164
Y. CİMTAY, Towards real time image dehazing on android operating system	177

C O M M U N I C A T I O N S

FACULTY OF SCIENCES
UNIVERSITY OF ANKARA

DE LA FACULTE DES SCIENCES
DE L'UNIVERSITE D'ANKARA



A STATISTICAL OVERVIEW ON SLEEP SCORING

Levent ÖZBEK¹, Levent SÜTÇİGİL², Hamdullah AYDIN³,
Sinan YETKİN⁴, Fuat ÖZGEN⁵

¹Ankara University, Faculty of Science, Department of Statistics, Ankara, Turkey

²Hasan Kalyoncu University, Faculty of Economics and Administrative Sciences, Department of
Psychology, G.Antep, Turkey

³Altınbaş University, Faculty of Economics and Administrative Sciences, Department of Psychology,
İstanbul, Turkey

⁴Sağlık Bilimleri University, Gülhane Medical Application and Research Center, Department of
Psychiatry, Ankara, Turkey

⁵Özel Bayındır Hospital, Clinic of Psychiatry, Ankara, Turkey

ABSTRACT. In this study, sleep electroencephalography (EEG) which is frequently used in statistical modelling has been modelled with the autoregressive (AR) time-series model and what kind of a structure the variance of the term *white noise* included in the model represented in different sleep stages has been observed. Taking all of the stages scored in accordance with Rechtschaffen and Kales criterion into account separately, epoches in each stage have been modelled with the AR and the variance of the term white noise in this model has been monitored. The study has evaluated the sleep EEG variances of a subject. In accordance with the results, the heterogeneity at Stage 2 was thought to be the reason why the objective differences appeared in scoring. It is thought that this data pointed out a necessity that the period in Rechtschaffen and Kales scoring which is called Stage 2 must be revised.

1. INTRODUCTION

Data analysis on electrophysiological phenomenon: macro and micro. Sleep scoring also need these type of approaches. Sleep has been described as the brother of death since the beginning of human being. At the beginning of 20th century, electrophysiological recording methods had revealed that changes body functions

Keyword and phrases. Sleep, EEG, time series

✉ ozbek@science.ankara.edu.tr; leventsutcigil@hku.edu.tr; hamdullah@uyku.gen.tr; smnyetkin@gmail.com
fuatozgen2000@yahoo.com

ORCID 0000-0003-1018-3114; 0000-0001-8147-0124; 0000-0002-3670-5040; 0000-0001-7708-2837; 0000-0001-7334-5817

could be recorded. Sleep studies based on basic electrophysiological methods. The first studies showed that brain functions have been changed during sleep. Rapid Eye Movement (REM) sleep discovered at 1953. after than sleep evaluated REM and NonREM (NREM) sleep. And than classification systems were described criteria to score sleep. After than Scientists have developed new and special methods. Especially, in the second part of 20th century, scientists have concentrated on microanalyses. Actually, high technology invited scientist to discover well known basic phenomenon. Actually, basic studies on sleep and related phenomenon had been discovered. Well known physiological changes were recorded, data analyses methods revealed relationship between physiological changes. All these studies revealed that intrinsic phenomenon have very close interaction. Especially, sleep studies have shown unknown phenomenon and interaction modellings. These approaches and mathematical modellings invited scientists get together especially in basic scientific areas.

Sleeping literally is the resting state in which consciousness towards the external stimuli was fully or partially lost, all kinds of activities decreased on a large scale and response strength was reduced. In medical terms, one may also include in the description that it is a different state of consciousness.

When Hans Berger recorded the electrical activity of human brain and revealed the presence of different rhythms between sleep and awareness in 1923, a new dimension has been added to researches on sleep [1]. Aserinsky and Kleitman have identified the eye movements during sleep and indicated them as a separate period in sleeping state [2]. On the other hand, Dement and Kleitman have identified the periodic phases during sleep in polysomnography studies they made using different physiological parameters [3].

Sleep scoring is an important step for the classification of the sicknesses and proper treatment practices in researching the patterns of sleep. Currently, Rechtschaffen and Kales classification is valid [4].

The Rechtschaffen and Kales classification has made important contributions to researches on sleep in the last thirty years. Along with its positive sides, the practice of scoring by an expert in epochs requires an intense labor and time. Rapidly-

changing micro structures and phase changes are unable to be evaluated in epochs lasting thirty seconds, and this leads to subjective differences in the evaluation. Making the classification with young and healthy subjects leads to an insufficiency in elderly subjects with sleep diseases, especially in those who have abnormal EEG structure caused by neurological diseases [5]. Looking at the disadvantages of the Rechtschaffen and Kales scoring criteria, studies on subgrouping the sleep phases have been made [6, 7]. To be able to make sleep scoring more objectively, data on EEG have been tried to be modelled with time series and the results of these models in different stages have been examined [8].

In this study, sleep EEG which is frequently used in statistical modelling has been modelled with the autoregressive (AR) time-series model and what kind of a structure the variance of the term *white noise* included in the model represented in different sleep stages has been observed.

Taking all of the stages scored in accordance with Rechtschaffen and Kales criterion into account separately, epochs in each stage have been modelled with the AR and the variance of the term white noise in this model has been monitored.

2. METHOD

A - Subject: A subject without any psychiatric complaints has been informed about the study and taken into polysomnographic examination for two nights in Sleep Researches Center of GATA Department of Mental Health and Diseases. In sleep records, the polysomnographer named Somnostar Alpha is used.

B - Polysomnographic examination: Each of the polysomnographic examinations has been scored in epochs lasting thirty seconds [4]. The EEG record (C3-A2) has been included in the evaluation at the second night.

C - Statistical method: Let it be considered that a dynamic system with the $\{y(t)\}$ output has been modelled with the linear difference equation of

$$y(t) = a_1 y(t-1) + a_2 y(t-2) + \dots + a_n y(t-n) + v(t).$$

Here, $\{v(t)\}$ shows the white noise process. The model above with the parameter vector $\theta^T = (a_1, \dots, a_n)$ and

$$\varphi(t)^T = (y(t-1), \dots, y(t-n))$$

is written as

$$y(t) = \theta^T \varphi(t) + v(t) \quad (1)$$

Regarding one of the most important problems in system identification, several methods on the estimation of the unknown parameter vector have been developed. There are problems encountered in cases especially when the system parameters and the variance of white noise process change over time, and for this reason, the estimators must be upgraded [9]. Kalman Filter which is one of the methods used to estimate the model parameters has been addressed in this study.

If the parameter vector is considered as a random walk model in dynamic linear model given by the Equality (1), the equality may be written as

$$\begin{aligned} \theta(t+1) &= \theta(t) + w(t) & w(t) &\square N(0, R_1(t)) \\ y(t) &= \varphi(t)^T \theta(t) + v(t) & v(t) &\square N(0, R_2(t)) \end{aligned} \quad (2)$$

in state space model form. Here, state vector is the parameter vector and transition matrix is the unit matrix. In these circumstances, depending on $\hat{\theta}(0)$ and $\hat{\theta}(0)$ initial values, KF is given by

$$K(t) = [P(t|t-1)\varphi(t)][\varphi(t)^T P(t|t-1)\varphi(t) + R_2(t)] \quad (3)$$

$$P(t|t-1) = P(t-1|t-1) + R_1(t) \quad (4)$$

$$e(t) = y(t) - \hat{y}(t) \quad (5)$$

$$\hat{y}(t) = \varphi(t)^T \hat{\theta}(t|t-1) \quad (6)$$

$$\hat{\theta}(t) = \hat{\theta}(t|t-1) + K(t)e(t) \quad (7)$$

$$P(t|t) = P(t|t-1) - K(t)\varphi(t)^T P(t|t-1) \quad (8)$$

[10]. In dynamic linear models, state and measurement noise covariances and variances must be known, in order to calculate the system state and make covariance estimations. Since values of these are mostly unknown, sequential estimations are

used. Under the assumption that the state noise covariance matrix in the Equation (2) is $R_1(t) = qI$, the parameter q is calculated by

$$q = h \left(\frac{e(t)^2 - E[e(t)^2 | q \equiv 0]}{\varphi(t)^T \varphi(t)} \right).$$

Here, it is formed as

$$h(x) = \begin{cases} x, & x \geq 0 \\ 0, & \text{else} \end{cases}$$

and

$$E[e(t)^2 | q \equiv 0] = R_2(t) + \varphi(t)^T P(t|t-1)\varphi(t).$$

With α indicating the correction parameter, the sequential estimation of the measurement noise variance of $R_2(t)$ is given by

$$R_2(t) = \alpha R_2(t-1) + (1-\alpha)h \left(e(t)^2 - \varphi(t)^T P(t|t-1)\varphi(t) \right) \quad (9)$$

and the sequential estimation of q is given by

$$\begin{aligned} q(t) &= \alpha q(t-1) + (1-\alpha)h \left(\frac{e(t)^2 - E[e(t)^2 | q \equiv 0]}{\varphi(t)^T \varphi(t)} \right) \\ &= \alpha q(t-1) + (1-\alpha)h \left(\frac{e(t)^2 - R_2(t) - \varphi(t)^T P(t|t-1)\varphi(t)}{\varphi(t)^T \varphi(t)} \right) \end{aligned} \quad (10)$$

[11]. The standard deviation and sleep histogram estimated in accordance with this method is shown in Figure 1.

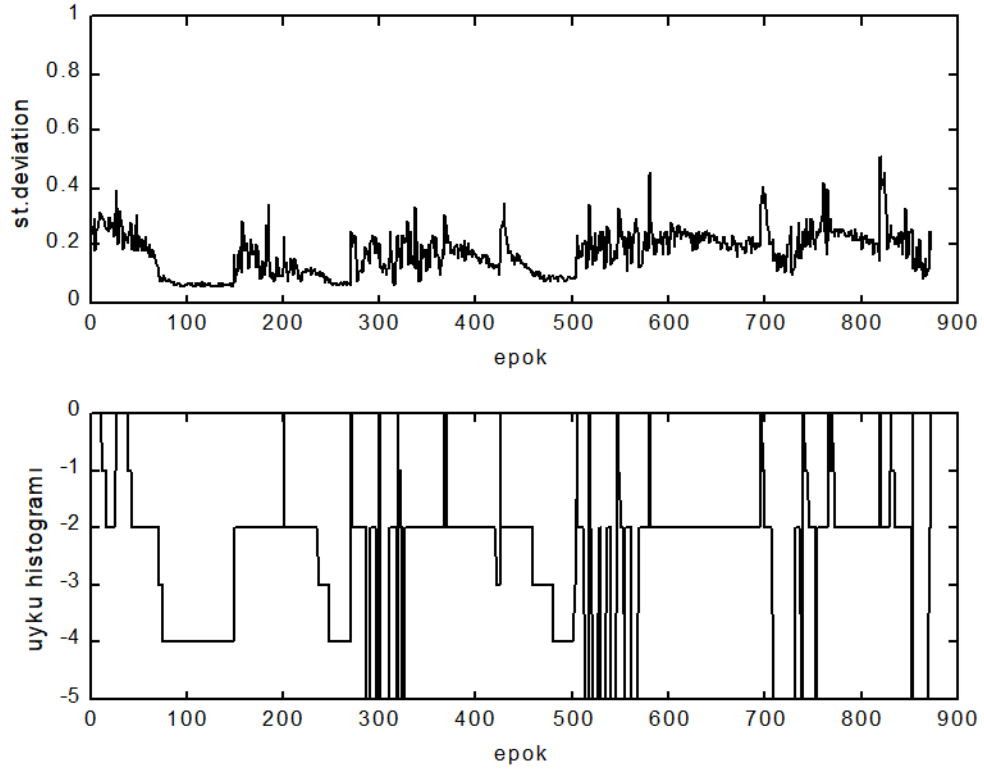


FIGURE 1. Sleep histogram and standard deviations

3. FINDINGS

In this study, the sleep EEG has been modelled as

$$y(t) = a_{1t}y(t-1) + e(t) \quad (11)$$

AR(1) process. a_{1t} in this model has been considered as parameter random walk process changing over time and calculated sequentially with the KF. The variance of white noise process in Equality (11) has been calculated adaptively by using (10) equality. In Figure 1, stages scored in accordance with the R-K criterion and the standard deviation of white noise variances in model corresponding to the stages have been shown.

At Stage 4, the variance was smaller than the other stages and it did not differ too much compared to varied epochs of Stage 4. At Stage 2, a big variance compared to Stage 4 has been encountered. When the variances of Stage 2 during the first half of the night and the Stage 2 during the second half of the night were observed, it is observed that the variance during the second half grew bigger.

4. RESULTS

The study has evaluated the sleep EEG variances of a subject. In accordance with the results given in Figure 2, the heterogeneity at Stage 2 was thought to be the reason why the objective differences appeared in scoring. It is thought that this data pointed out a necessity that the period in Rechtschaffen and Kales scoring which is called Stage 2 must be revised.

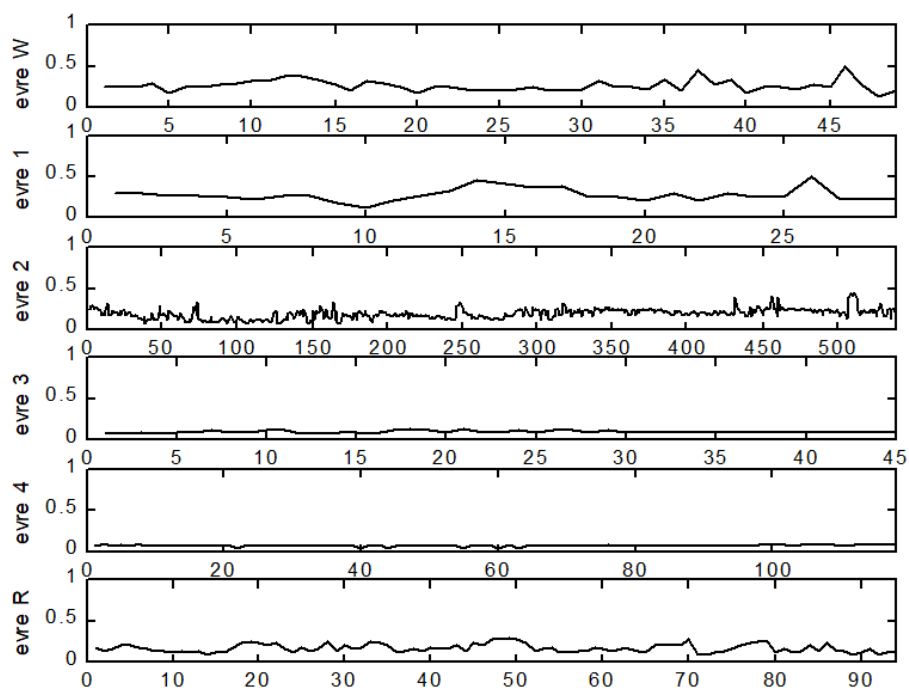


FIGURE 2. Standard deviations by stages

REFERENCES

- [1] Berger, H., Ueber das Elektroenkephalogramm des Menschen, *J. Psychol. Neurol*, 40 (1930), 160-179.
- [2] Aserinsky, E., Kleitman, N., Regularly occurring periods of eye motility and concomitant phenomena during sleep, *Science*, 118 (1953), 273-274. <https://doi.org/10.1016/j.jqsrt.2012.05.012>.
- [3] Dement, W., Kleitman, N., Cyclic variations in EEG during sleep and their relation to eye movements, body motility and dreaming, *EEG Clin. Neurophysiol.*, 9 (1957), 673-690.
- [4] Rechtschaffen, A., Kales, A., A manual of Standardized Terminology Techniques and Scoring System for Sleep Stages of Human Subjects, Brain Information Service/ Brain Research Institute, University of California, Los Angeles, 1968.
- [5] Bazil, C.W., Castro, L.H., Walczak, T.S., Reduction of rapid eye movement sleep by diurnal and nocturnal seizures in temporal lobe epilepsy, *Arch. Neurol.* 57 (2000), 363-368.
- [6] Hori, T, Hayashi, M, Morikowa, T., Topographic EEG changes and the hypnagogic experience, Ogilvie, R.D., Harsh, Jr. (eds). *Sleep Onset: Normal and Abnormal Processes*, Washington, American Psychological Association, 1994.
- [7] Lubin, A, Johson, L.C., Austin, M.T., Discrimination among states of consciousness using EEG spectra, *Psychophysiol.*, 6 (1969) 122-132.
- [8] Olbrich, E, Achermann, P., Oscillatory events in the human sleep EEG- detection and properties, *Neurocomputing*, 58 (2004), 129-135.
- [9] Özbek, L., Aliev, F.A., Adaptive Fading Kalman Filter with an Application, *Automatica*, 12 (1998), 1663-1664.
- [10] Özbek, L., Kalman Filtresi, Akademisyen Yay., 2017.


ANALYZING THE PERFORMANCE OF PURE LATERATION IN INDOOR ENVIRONMENTS WITH VARIOUS PERFORMANCE METRICS

Korhan CENGİZ

Department of Electrical-Electronics Engineering, Faculty of Engineering, Trakya University, Edirne,
TURKEY

ABSTRACT. Nowadays, determining the location of the users and devices in indoor buildings is promising research topic. Accurate position determination of the users for indoor environments is used for numerous applications such as public safety, supermarkets, health care applications, travelling, social networks and tourism. However, global positioning systems created for outdoor localizations cannot be used for indoor positioning systems (IPS) because detecting the exact position of a target is an issue for IPS. For indoor environments, there are several positioning algorithms such as lateration, fingerprinting, dead reckoning etc. Lateration is low cost and easy to deploy when compared to other existing algorithms. Therefore, in this study, received signal strength based pure lateration that uses synthetic data generated from MATLAB is proposed. The performance of pure lateration is investigated in terms of several performance metrics such as effect of varying number of the access points (AP), varying dimensions of the measurement area, varying Gaussian Noise power and varying number of test points in the field. The simulation of the pure lateration algorithm is conducted in MATLAB. The effect of the performance metrics are investigated and discussed in details. According to the results, accuracy performance of lateration is increased when the number of APs increase in the area, however this will bring some hardware costs. In addition, when the number of test points increases in the field, in other words the step size between two test points decreases in the field the error performance of lateration is also enhanced however, this will also cause to computational costs. Finally, enlarging the measurement area causes to decrease the accuracy performance of lateration as expected. The main purpose of this study is to obtain the optimum conditions for lateration to provide a solution for real time applications. For future work, the real time implementations of this study are performed and to improve the accuracy performance, it is aimed to use a curve fitting idea to the measured values.

Keyword and phrases. Pure lateration, indoor positioning, triangulation, GPS.

 korhancengiz@trakya.edu.tr
 0000-0001-6594-8861

1. INTRODUCTION

Recent years, the determination of location of a device has become an important requirement in numerous applications. Global Positioning System (GPS) has become fully useful in 1995. The GPS is a space-based satellite navigation system that provides position and time information in all conditions, anywhere where there is an unobstructed line of sight to three or more GPS satellites [1]. The GPS includes triangulation technique to detect physical positions of the users in outdoor environments. On the other hand it is not useful for exact determination of the locations of the users in indoor environments [2]. The concrete walls cause to attenuation of the signals transmitted from satellites and thus the signals do not penetrate walls. Thus, finding the location of a target in a building becomes unfeasible.

In recent years, according to the enhancements in the technologies, people pass the time of day in indoor environments therefore the demand for indoor positioning technologies arises. In these indoor buildings, people can use IPS to arrive gate in an airport, patient services in hospitals or products in supermarkets. With prospering actualizations of the IPSs, a variety of applications can be realized for indoor places [3]. To illustrate, safety, social network and health care applications can be performed by using IPS. In addition, as instance, indoor localization technique can also ensure innovative and accurate ways to find out the position of a person in a building in the event of a disaster because person's life matter, gaining some time during this kind of an event, is so critical [4].

Latterly, IPS becomes a popular research field because of the above mentioned implementations thus many research and publications have been made in IPS field. Various IPS studies are proposed by authors [5]. In a Received Signal Strength (RSS)-based localization system [6] the position of a target can be found by calculating the distance of an object from the transmitter using triangulation or lateration approaches.

The well-known approaches using for signal measurements are: Angle of Arrival (AOA), Time of Arrival (TOA), Time Difference of Arrival (TDOA) and Received Signal Strength Indicator (RSSI) [3]. AOA [7] needs computation of the angles at which the signals arrive from the un-located device to the anchor nodes. This scheme only requires two measuring units for 2D-positioning and it does not require synchronization between the measurement units. AOA can be utilized ably when LOS appears but the accuracy diminishes in multi-path environments. TOA utilizes the distances between the transmitting nodes and the receiving nodes from the

transmission time delays and the corresponding speed of the signals to find out the positions of the objects [8, 9]. TOA ensures high precision, however, it causes to extra cost because of the high hardware complexities. TDOA technique also uses distance-based measurements to determine the positions of the objects [10]. They find the relative locations of the transmitters based on the variation of the TOA of the propagation of the signals in the transmitters and multi-sensors. When the signal reaches to two reference points, the difference in arrival time can be used to calculate the differences of the distances between the object and the two reference points. It is less complicated than TOA and it fulfils notable certainty performances.

Value of a RSSI is the measure of the power level of RSS. It is measured by decibel-milliwatt (dBm) that corresponds to a negative number. If the received signal reaches strong the value becomes closer to zero. To find out the position of an object with RSSI, the RSSI values between the sensors attached to a target user and enclosing access points (APs) with pre-defined positions should be measured [11]. The combinations of these multiple RSSI values can be utilized to compute the approximate location of the target. Frequently, at a minimum 3 APs are needed to find out the location of a target. The positions of the targets are acquired by calculating the distances of the objects from senders by the help of tri-angulation or tri-lateration techniques. RSSI based localization is easy to use by comparison with the techniques that use AOA and TDOA [12]. For RSSI methods, particular equipment both at the cell-phones and the wireless interface cards are not needed to be utilized [13].

2. PURE LATERATION TECHNIQUE

Location detection by the help of distance measurements using signal strengths is named as lateration. This scheme is used in IPS due to its preciseness and cheapness. The lateration techniques are based on position information of the reference points and the distances to them.

Firstly, to find the accuracy error of pure lateration, the RSSI Matrix which includes noisy RSSI measurements of APs on each test point in a room can be defined as shown below:

$$X_{RSSI} = \begin{bmatrix} RSSI_{(1,1)} & \cdots & RSSI_{(1,T)} \\ \vdots & \ddots & \vdots \\ RSSI_{(K,1)} & \cdots & RSSI_{(K,T)} \end{bmatrix} \quad (1)$$

Here, T corresponds to number of test points in the measurement area and N denotes the number of APs in the field. As instance, T can be 196 and K can be 4. The distance of an object from the transmitter can be computed by using (2) given below, after measuring the received power at the target position given that A and n values are known:

$$r_p = 10^{\frac{A - X_{RSSI}(x,y)}{10n}} \quad (2)$$

In here, A value shows the power of an AP in dBm and n corresponds to the path loss exponent of the environment. By using rP values and following two equations, Eq. (5) can be obtained:

$$C_{act} = \begin{bmatrix} 2(x_2 - x_1) & 2(y_2 - y_1) \\ \vdots & \vdots \\ 2(x_K - x_1) & 2(y_K - y_1) \end{bmatrix} \quad (3)$$

$$D = \begin{bmatrix} r_{p1}^2 - r_{p2}^2 + x_2^2 + y_2^2 - x_1^2 - y_1^2 \\ \vdots \\ r_{p1}^2 - r_K^2 + x_K^2 + y_K^2 - x_1^2 - y_1^2 \end{bmatrix} \quad (4)$$

$$\begin{bmatrix} x_{est} \\ y_{est} \end{bmatrix} = (C_{act}^T C_{act})^{-1} C_{act}^T D \quad (5)$$

Eq. (5) shows the estimated locations of the pure lateration method. To find the estimated error in each test point, the difference between estimated locations and actual locations can be used as shown in (6):

$$e = \begin{bmatrix} x_{est} \\ y_{est} \end{bmatrix} - \begin{bmatrix} x \\ y \end{bmatrix} \quad (6)$$

3. RESULTS

Simulations and analyses of pure lateration are conducted in MATLAB. The results of simulations and discussions are presented in this section. Varying number of access points (APs), varying step sizes and Gaussian Noise parameters are used to obtain several simulation results.

Fig. 1 illustrates the error value of each test point of pure lateration under low Gaussian Noise (standard deviation of noise is 2). Here, there are 196 test points and 4 APs which are located at the corners of measurement field. The dimensions of the

field are 6m x 6m. From this figure, it is obtained that lateration error increases especially when the test points are very close to the APs. The whole distribution of the lateration error on each point can be obtained from this figure. Note that, in here the average lateration error is approximately 1.3321 m.

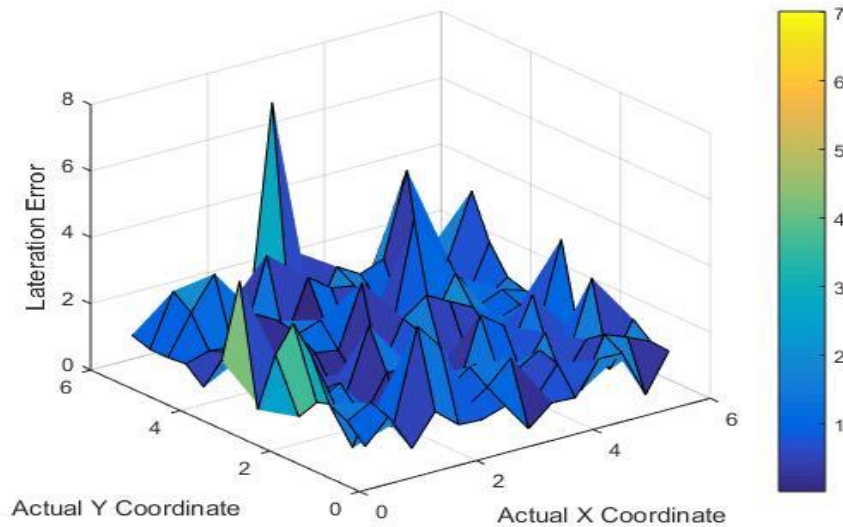


FIGURE 1. Lateration error distribution of each point under low Gaussian Noise

Fig. 2 illustrates the error distribution of each test point of pure lateration under lower Gaussian Noise (standard deviation of noise is 1). Here, there are 196 test points and 4 access points which are located at the corners of measurement field. The dimensions of the field are 6m x 6m. From the figure, it is obtained that lateration error increases especially when the test points are very close to the APs. The whole distribution of the lateration error on each point can be obtained from this figure. Note that, in here the average lateration error is approximately 0.5869 m. The average error is decreased dramatically when the noise is decreased.

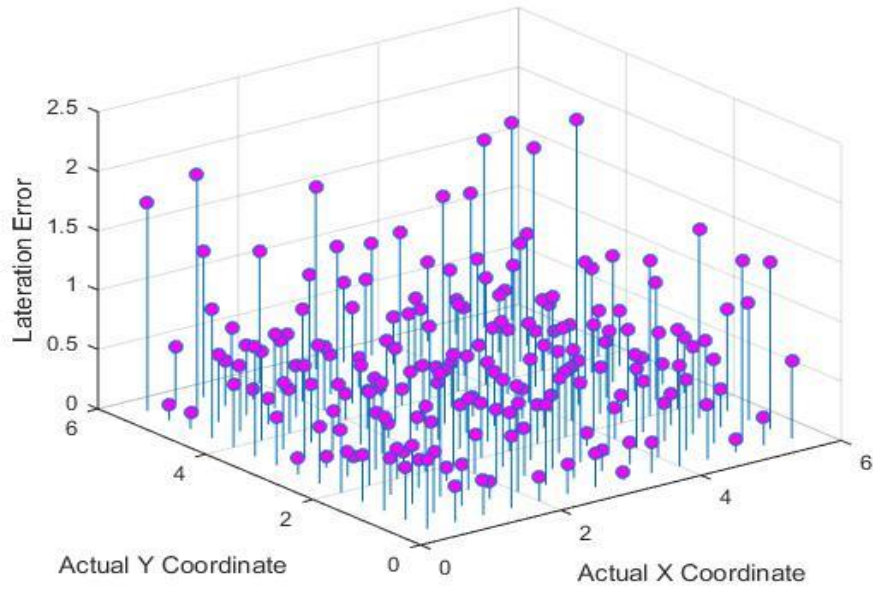


FIGURE 2. Lateration error distribution of each point under lower Gaussian Noise

To investigate the effect of Gaussian Noise on pure lateration, the simulations are conducted for varying Gaussian Noise values. Fig. 3 shows the average error performance of pure lateration in term of varying Gaussian Noise. The average error increases when the noise increases in the system as expected.

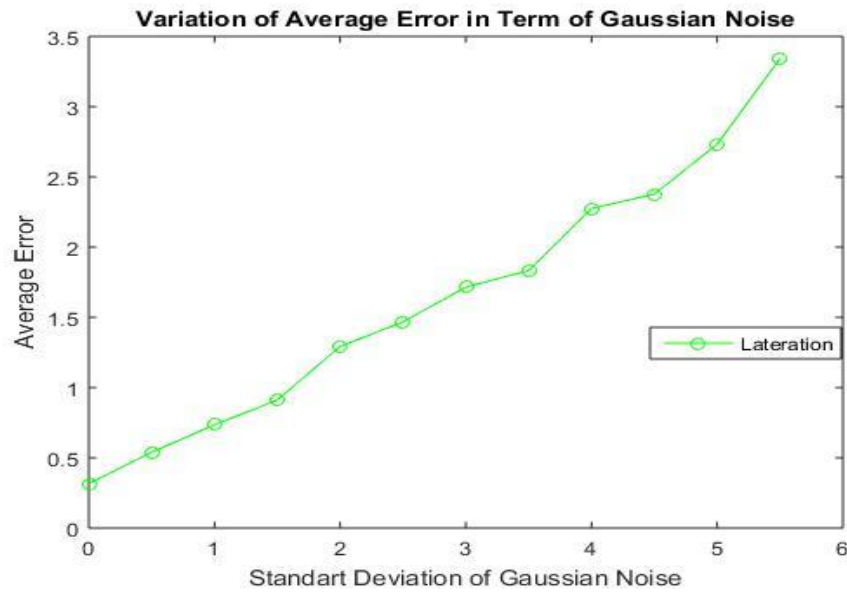


FIGURE 3. Average lateration error according to different noise values

Under low Gaussian Noise (standard deviation of 2), the performance of pure lateration is also investigated in this study. Fig. 4 illustrates the average error value of each iteration of pure lateration under 100 independent iterations. Here, there are again 4 APs, 196 test points in 6m x 6m measurement area. According to the results, the average error performance of lateration varies between 1.2 m and 1.5 m.

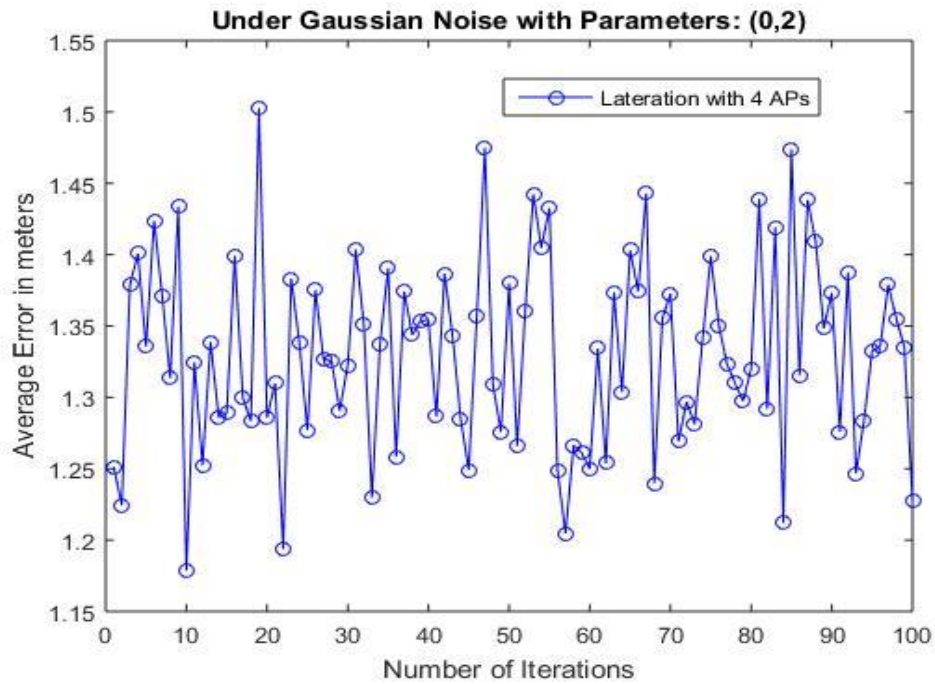


FIGURE 4. Average error performance of lateralation with iterations

Table 1 shows the variation of lateralation error according to varying number of APs under 100 independent iterations. Here, there are 196 test points and noise parameter is 2 in 6m x 6m field. According to these simulation results, it is obtained that, when the number of APs increase in the measurement area, the error performance of pure lateralation enhances. However, increasing the number of APs brings extra computational, hardware and financial costs to the designers and researchers.

TABLE 1. Average lateralation errors according to different number of access points

Number of APs	Average Lateralation Error in meters
3	1.6925
4	1.3182
6	1.2301
8	1.1324

Table 2 shows the variation of lateration error according to different room sizes for 100 independent iterations. Here, there are 196 test points and noise parameter is 2. According to these simulation results, it is obtained that, when the room size (measurement area) is enlarged the accuracy performance of pure lateration decreases as expected. This problem can be solved by using more number of test points in other words using lower step size parameter or increasing the number APs in the field as illustrated in Table 1.

TABLE 2. Average lateration errors according to varying field dimensions

Field Dimensions	Average Lateration Error in meters
3m x 3m	0.6001
6m x 6m	1.3257
12 m x 12 m	2.6913
18 m x 18 m	4.0724
24 m x 24 m	5.4321

Table 3 shows the error performance of pure lateration for the parameters: 4 APs and 196 TPs under 100 independent iterations. As expected and discussed above, when the noise increases in the measurement environment, the accuracy performance of pure lateration decreases dramatically.

TABLE 3. Average lateration errors according to varying Gaussian noise

STANDART DEVIATION VALUE OF GAUSSIAN NOISE	AVERAGE LATERATION ERROR IN METERS
0.05	0.0304
0.2	0.1227
0.5	0.3062
1	0.6205
2	1.3229
4	3.3409
5	4.9849

3. CONCLUSIONS

Detecting the locations of the users in buildings has been an important research topic recent years. IPS can be utilized a variety of fields such as, shopping applications, social platforms, logistics, tourism sectors and transportation. However, GPS is designed for outdoor places, is not proper for IPS, making certain location determination a extorsive issue for IPS. In this study, pure lateration method that uses existing infrastructure, is proposed. By increasing the number of APs, the pure lateration technique improves the precision of location estimations. The usage of the existing substructure turns the designed method into cheaper when comparing with existing solutions that need pricy components. The proposed method is investigated under different performance metrics in MATLAB. The results of the simulations are evaluated and discussed in details to determine the optimum solution of pure lateration in indoor environments. As a future work, it is planned to use polynomial fitting algorithms to enhance the accuracies of the lateration schemes.

REFERENCES

- [1] Koyuncu, H., Yang, S., A Survey of Indoor Positioning and Object Locating Systems, *IJCSNS International Journal of Computer Science and Network Security*, 10(5) (2010), 121-128.
- [2] Gezici, S., A survey on wireless position estimation, *Wireless Personal Communications*, vol. 44, pp. 263-282, 2008.
- [3] Sakpere, W., Adeyeye, O., Mlitwa, N., A State-of-the-Art Survey of Indoor Positioning and Navigation Systems and Technologies, *South African Computer Journal*, 2(3) (2017), 145–197.
- [4] Yassin, A. et al., Recent Advances in Indoor Localization: A Survey on Theoretical Approaches and Applications, *IEEE Communications Surveys & Tutorials*, 19(2) (2017), 1327-1346.
- [5] Zhang, D. et al., Localization Technologies for Indoor Human Tracking, *Proc. of 5th International Conference on Future Information Technology*, (2010).
- [6] Mounir, T. et al., Positioning system for emergency situation based on RSSI measurements for WSN, *Proc. of International Conference on Performance Evaluation and Modeling in Wired and Wireless Networks (PEMWN)*, (2017).
- [7] Lee, Y., Weighted-average based aoa parameter estimations for LR-UWB wireless positioning system, *IEICE Transactions on Communications*, 94 (2011), 3599-3602.
- [8] Alsindi, N., Alavi, B., Pahlavan, K., Spatial characteristics of UWB TOA based ranging in indoor multipath environments, *Proc. of 18th IEEE international symposium on personal, indoor and mobile radio communications*, pp. 1-6, Athens, Greece, 2007.
- [9] Alsindi, N.A., Alavi, B., Pahlavan, K., Measurement and modeling of ultrawideband TOA-based ranging in indoor multipath environments, *IEEE Transactions on Vehicular Technology*, 58 (2009), 1046-1058.

- [10] Reddy, N., Sujatha, B., TDOA computation using multicarrier modulation for sensor networks, *International Journal of Computer Science Communication Network*, 1 (2011), 85-90.
- [11] Obeidat, H. et al., Indoor localization using received signal strength, *Proc. of 8th IEEE Design and Test Symposium*, 2013.
- [12] Youssef, M. Agrawala, A., Shankar, A.U., WLAN location determination via clustering and probability distributions, *Proc. of IEEE International Conference on Pervasive Computer Communications (PerCom)*, (2003), 143-150.
- [13] Bahl, P., Padmanabhan, V.N., RADAR: an in-building RF-based user location and tracking system, *Proc of IEEE Infocom, Tel Aviv Israel*, (2000), 775-784.

LPI RADAR WAVEFORM CLASSIFICATION USING BINARY SVM AND MULTI-CLASS SVM BASED ON PRINCIPAL COMPONENTS OF TFI

Almila BEKTAŞ and Halit ERGEZER



Çankaya University, Mechatronics Engineering Department, Ankara, TURKEY

ABSTRACT. Since cognition has become an important topic in Electronic Warfare (EW) systems, Electronic Support Measures (ESM) are used to monitor, intercept and analyze radar signals. Low Probability of Intercept (LPI) radars are preferred to be able to detect targets without being detected by ESM systems. Because of their properties as low power, variable frequency, wide bandwidth, LPI Radar waveforms are difficult to intercept with ESM systems. In addition to intercepting, the determination of the waveform types used by the LPI Radars is also very important for applying counter-measures against these radars. In this study, a solution for the LPI Radar waveform recognition is proposed. The solution is based on the training of Support Vector Machine (SVM) after applying Principal Component Analysis (PCA) to the data obtained by Time-Frequency Images (TFI). TFIs are generated using Choi-Williams Distribution. High energy regions on these images are cropped automatically and then resized to obtain uniform data set. To obtain the best result in SVM, the SVM Hyper-Parameters are also optimized. Results are obtained by using one-against-all and one-against-one methods. Better classification performance than those given in the literature has been obtained especially for lower Signal to Noise Ratio (SNR) values. The cross-validated results obtained are compared with the best results in the literature.

1. INTRODUCTION

Electronic Warfare (EW) systems are involved in LPI Radars as they are unlikely to intercept and it is hard to analyse them in detail while they track the targets [1]. By using the information provided by ES systems, Electronic Counter Measures (ECM)

Keyword and phrases. Low probability of intercept radar, support vector machine, principal component analysis

 a.bektas@cankaya.edu.tr; halitergezer@cankaya.edu.tr
 0000-0002-5253-7825; 0000-0002-7280-0416

© 2020 Ankara University
Communications Faculty of Sciences University of Ankara Series A2-A3: Physical Sciences and Engineering

are used for interfering the radar operation by providing false information and noise, that is why LPI Radar waveform recognition is very important for EW systems.

Different techniques are used to insert signal data into the classifiers such as using raw data, filtered data [2], arrays or Time-Frequency Images. Some of the Time-Frequency Analysis (TFA) techniques used for LPI Radar waveform recognition are Choi Williams Distribution (CWD) [1], [3] - [7], Wigner-Ville Distribution (WVD) [1], [4], [7], Radon-WVD [8], short-time Fourier Transform (STFT) [9] and discrete Fourier Transform(DFT) [10]. By using results obtained from these distributions, images that show various frequency over time are generated. These images are called Time-Frequency Images. In literature, the commonly used TFA technique for LPI Radar waveform recognition is CWD because WVD-TFI contains interfering ghost terms and these terms degrade the performance of classification. The effect of different TFA techniques on LPI Radar classification may be the subject of another study. Similar to the ones in the literature, TFIs used in this paper are generated by using CWD. Unlike the methods given in the literature, during the generation of TFIs simple operations that do not require much processing time are performed. While converting the time-frequency graph of the CWD transform, the appropriate parameters used to improve image quality and pixel values are normalized to clarify the distinctive features.

Various techniques have been proposed for classification by using Time-Frequency Images. As a LPI Radar Waveform Recognition Technique [3], [6] uses the Convolutional Neural Network (CNN). The computational cost has become a problem because of the generated TFI sizes. [3] proposes a sampling averaging technique (SAT) which provides a higher sampling rate with a lower computational cost. However, because of the CNN complexity, TFIs are re-sized by using nearest-neighbour interpolation. But by using interpolation, some distinctive features of TFIs may be lost. Instead of this, taking the principal components of the signals that carry most of the information is a more accurate way to decrease computational complexity. It is indicated in [3] that to reduce the number of signal samples, consecutive signal samples are averaged by applying coherent summation, but it is not clear how to guarantee coherency in real-world applications and the effect of coherency on the performance of classification. In this paper, to reduce the computational cost of TFA, Fractional Fourier Transform is utilized. [8] uses Wigner Ville Distribution (WVD) to obtain TFI. Before creating WVD-TFIs, a basic threshold was applied to the amplitude of the signals to fix the raised spikes that the phase changes caused. As a classification technique, they propose the Fractional Fourier transform (FRT) to reduce the computational cost. Proposed LPI Radar waveform recognition technique excludes the four Poly-time signals (T1, T2, T3, T4). The classification performances of [7] are lower than other techniques, although

they classified fewer signal types than others. [4] uses a single-shot multi-box detector (SSD) to detect both Continuous Wave (CW) and Pulse Wave(PW) signals and a supplementary classifier to classify signals that cannot be classified using SSD. In [4], it is mentioned that LPI waveform recognition has been performed for both CW and Pulsed Signals. It is also stated that recognition of CW LPI signals is challenging due to the lower peak power values of CW signals. However, when we evaluate the CW and Pulsed signals having the same average power value, CW signals are clearly distinguishable and traceable in TFI as a continuous curve along the *time axis*. This is not the case for Pulsed signals. For Pulsed signals, small zones of high intensity are observed in certain regions of the TFI. In our study, CW signals are not considered for classification, but our approach can also be applied to CW signals. The rationale behind this is that the highest energy region along the *time axis* is selected during the automatic crop of the respective zones in the TFI. Therefore, it becomes clear that the average power of the signal is important, not the peak power. LPI Radar waveform recognition techniques based on multi-layer perceptron, radial basis function and probabilistic neural networks are utilized in [7]. To minimize the information loss, classification is done based on deep sparse capsule networks in [11] and they used cross ambiguity functions for feature extraction. [5] proposed an image fusion algorithm and used CNN for feature extraction. Yet, poly-phase Frank code was excluded in classification. As a result, the similarity between Frank and other poly-phase codes is not examined. In this case, to compare [5] with other techniques that include both poly-phase codes and Frank code does not give an accurate result. Also, clustering [9], decision trees and SVM [5], [12] are commonly used techniques for classification.

In this paper Linear Frequency Modulation (LFM), Costas, Binary Phase Shift Keying (BPSK), Frank, P1, P2, P3, P4, T1, T2, T3, T4 signals are used for classification. Time-frequency images are generated using Choi-Williams Distribution [13].

All images are cropped automatically to make them include maximum information and then resized to a constant dimension for all signals to keep data vectors uniform. SVMs are used to train the dataset. Both binary classification and multi-class classification methods are used. For multi-class classification, Directed Acyclic Graph SVM (DAGSVM) method is used which is based on Decision Directed Acyclic Graph (DDAG) [23].

Support Vector Machine is an effective classification algorithm that is suitable for LPI Radar classification due to its good generalization performance. A major limitation of SVM is the high demand for memory during training. To overcome this limitation, Principal Component Analysis (PCA) is applied to TFIs. Unlike other

methods proposed in the literature, principal components have been used instead of resizing the images that cause entropy increase.

There are a lot of parameters to be turned in SVMs such as choosing the "right" kernel, regularization penalties, and the slack variable. These parameters must be optimized to find the best generalization. Firstly, SVMs are trained by using different Kernel Functions. We notice that different types of LPI signals can be classified better with different Kernel Functions. Then, it is decided to apply Hyper-Parameter Optimization to the Kernel Functions as well. Therefore, the optimal Kernel Function selection is automatically done by Hyper-Parameter Optimization. Then, the optimal parameter sets are used for each SVM. 5-fold cross-validation results of both binary classification and multi-class classification methods are presented. For both of the methods, the same folds are used to be able to compare the performance of binary classification method and multi-class classification method. All SNR values of TFIs between -20dB to 10dB are uniformly distributed and fairly separated between folds.

The paper is organized as follows. Firstly, the mathematical expressions are given in Section 2. The TFA technique used in the proposed solution is expressed and LPI Radar Signal TFIs are shown in Section 3. Then, the proposed solution is explained in detail in Section 4. Section 5 contains the results and comparisons with results in the literature and then all sections are concluded in 6.

2. LPI RADAR SIGNALS

Mathematical explanations of LPI Radar signals used for the proposed solution are given below.

A. Frequency Modulation Continuous Wave (FMCW)

Frequency modulation of FMCW signals is created by using increasing and decreasing frequency signals. Increasing and decreasing frequencies f_i and f_d are [1]:

$$f_i = \left(f_0 - \frac{\Delta F}{2}\right) + \frac{\Delta F}{t_m} t \quad (1)$$

$$f_d = \left(f_0 + \frac{\Delta F}{2}\right) - \frac{\Delta F}{t_m} t \quad (2)$$

respectively, where f_0 is the carrier frequency, t is time, ΔF is modulation bandwidth and t_m is modulation period. The modulation bandwidth of 250, 500, 750 and 1000Hz are used to generate FMCW signals.

B. Binary Phase Shift Keying (BPSK)

Phase modulation of the BPSK signal is provided by Barker Sequences with various lengths. A Barker Sequence $B = [b_0, b_1, \dots, b_n]$ contains +1's and -1's of length $n \geq 2$. In this paper, Barker Sequence length of 7, 11 and 13 are used to generate BPSK signals.

C. Costas

Costas signal contains a set of frequencies that are chosen from the available frequencies $f_1, f_2, f_3, \dots, f_m$. Frequency modulation of the carrier signals is provided by the set [22]. When creating the dataset to train SVMs, 3 different sets of frequencies with different lengths are used.

D. Polyphase

Polyphase signals' modulation is applied by phase functions given in equations (4) to (7). In order to approach a stepped or linear frequency modulation, the number of phase states is varied and the time spent at each phase state is constant. 5 different phase functions for polyphase signals are given [22]:

Frank

$$\Phi_{FR}(i, j) = \frac{2\pi}{N_p} (i - 1)(j - 1) \quad (3)$$

P1

$$\Phi_{P1}(i, j) = \frac{-\pi}{N_p} (N_p - (2j - 1)) ((j - 1)N_p + (i - 1)) \quad (4)$$

P2

$$\Phi_{P2}(i, j) = \left\{ \frac{\pi}{2} \left[\left(\frac{N_p - 1}{N_p} \right) - \left(\frac{\pi}{N_p} \right) (i - 1) \right] \right\} [N_p + 1 - 2j] \quad (5)$$

where $i, j=1 \dots N_p$. N_p is the number of phase states.

P3

$$\Phi_{P3}(k) = \frac{\pi}{N_p} (k - 1)^2 \quad (6)$$

P4

$$\Phi_{P4}(k) = \left(\frac{\pi}{N_p} (k-1)^2 - \pi(k-1) \right), \quad (7)$$

where $k=1, \dots, N_p$ and N_p is the number of phase states.

E. Polytime

As it is stated earlier in the Polyphase section, the time spent at each phase state is constant. In Poly-time signals the number of phase states is user-defined and the time spent at the phase states is varied to approach a stepped or linear frequency modulation. Phase functions of Poly-time codes are [1]:

T1

$$\Phi_{T1}(t) = \text{mod} \left\{ \frac{2\pi}{N_p} \left[(mt - jT) \frac{jN_p}{T} \right], 2\pi \right\} \quad (8)$$

T2

$$\Phi_{T2}(t) = \text{mod} \left\{ \frac{2\pi}{N_p} \left[(mt - jT) \left(\frac{2^{j-m+1}}{T} \right) \frac{N_p}{2} \right], 2\pi \right\} \quad (9)$$

T3

$$\Phi_{T3}(t) = \text{mod} \left\{ \frac{2\pi}{N_p} \left[\frac{N_p \Delta F t^2}{2t_m} \right], 2\pi \right\} \quad (10)$$

T4

$$\Phi_{T4}(t) = \text{mod} \left\{ \frac{2\pi}{N_p} \left[\frac{N_p \Delta F t^2}{2t_m} - \frac{N_p \Delta F t}{2} \right], 2\pi \right\}, \quad (11)$$

where $j = 0, 1, 2, \dots, m-1$ and m is the number of frequency segments, N_p is the number of phase states and T is overall code period.

3. TIME-FREQUENCY ANALYSIS TECHNIQUE: CHOI-WILLIAMS DISTRIBUTION

Choi Williams Distribution (CWD) [13], [14] has been used to create time-frequency images of the LPI Radar signals. It is a time-frequency analysis technique that is used to extract data from the signal. CWD is included in Cohen's generalized class as a time-frequency distribution. It uses an exponential kernel function while Wigner-Ville Distribution (WVD) uses a kernel as one. The exponential kernel function makes CWD different than other distributions. CWD is expressed in discrete form as:

$$CWD_x(t, \omega) = 2 \sum_{\tau=-\infty}^{\infty} e^{-j2\omega\tau} \sum_{\mu=-\infty}^{\infty} \frac{1}{\sqrt{4\pi n^2/\sigma}} e^{-\sigma(\mu-t)^2/(4\tau^2)} x(\mu + \tau)x^*(\mu - \tau) \quad (12)$$

where t is the time index, ω is the angular frequency, $x(\mu)$ is the time signal and $x^*(\mu)$ is its complex conjugate, τ is the time delay and σ is scaling factor [15].

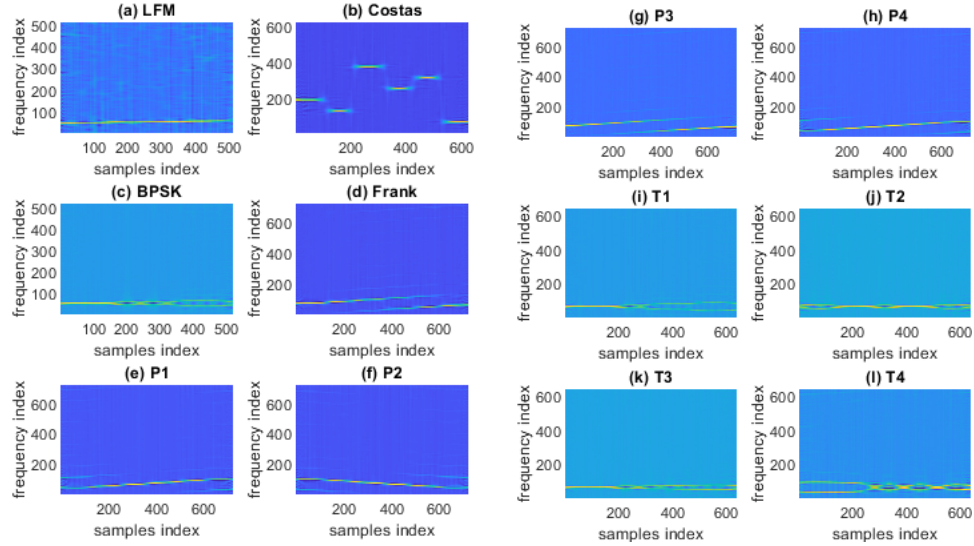


FIGURE 1. 12 LPI Radar signals TFIs that are created by using CWD. All signals created with a SNR value of 0dB.

CWD images of each LPI Radar signal and No-Modulation signal have created at 16 different SNR values, which varies -20dB to 10dB with a step of 2dBs. All of the signals are created 20 different times with 20 different random noises to make the effect of noise more realistic. It is mentioned in Section 2 that some of the signals

are created with different parameters. In Figure 1, 12 different LPI Radar signals at 0dB are shown.

4. PROPOSED LPI RADAR WAVEFORM CLASSIFICATION TECHNIQUE

The block diagram of the proposed technique is given in Figure 2. To recognize 12 different LPI waveforms given in Section 2 and the No-Modulation signal, signals are sampled at a sampling rate of 20 kHz. Then, Choi Williams Distribution is applied to the sampled data. The output CWD-TFI is automatically cropped according to the high energy regions on the image. Cropped images are resized to a fixed size in order to provide uniformity when creating the dataset. This process has been repeated for every image which has different waveforms, parameters and SNR values. A total of N ($=33600$) images have been created in RGB format, each with a dimension of 64×64 pixels. The resulting RGB images are transformed into feature vectors of size M ($=64 \times 64 \times 3 = 12288$). Since we have used RGB format instead of transforming TFIs into greyscale images, distinctive features of TFIs are preserved. All feature vectors are collected into a $N \times M$ matrix to create the dataset which is the input of PCA. With the application of PCA, a new $N \times K_e$ dataset matrix is created using the features that contain the highest information. K_e is the number of features with the highest information in the feature vector. By this way, the data load is reduced. These principal components are used to train SVM. For one-against-all SVMs, the signal type to be trained is labelled as +1 and all other signal types are labelled as -1. For example, to train SVM for BPSK, the BPSK images are labelled as +1, other classes corresponding to 11 LPI signal types and No-Modulation signal are labelled as -1. While training the classifier, the parameters including kernel types and kernel parameters are optimized to obtain the best scenario. For each signal type, 5 SVMs are trained by 5-fold cross-validation. A total of 65 SVMs are trained for one-against-all method and a total of 390 SVMs are trained for one-against-one method. At the end of this process, we have PCA centres and trained classifier.

SVM is an algorithm that is generally used to classify the data with a boundary. The total distance between the closest feature vectors of both and the boundary is called margin. Assume (x_i, y_i) is a feature vector where x_i is the feature and y_i is the class label for $i = 1, 2, \dots, N$. $x_i \in IR^p$ and $y_i \in \{-1, 1\}$.

A hyperplane is defined by

$$\{x: f(x) = x^T \beta + \beta_0 = 0\} \quad (13)$$

where β is a unit vector. Classification rule is:

$$G(x) = \text{sign}[x^T \beta + \beta_0]. \quad (14)$$

The correct classification satisfies $y_i f(x_i) > 0 \forall_i$.

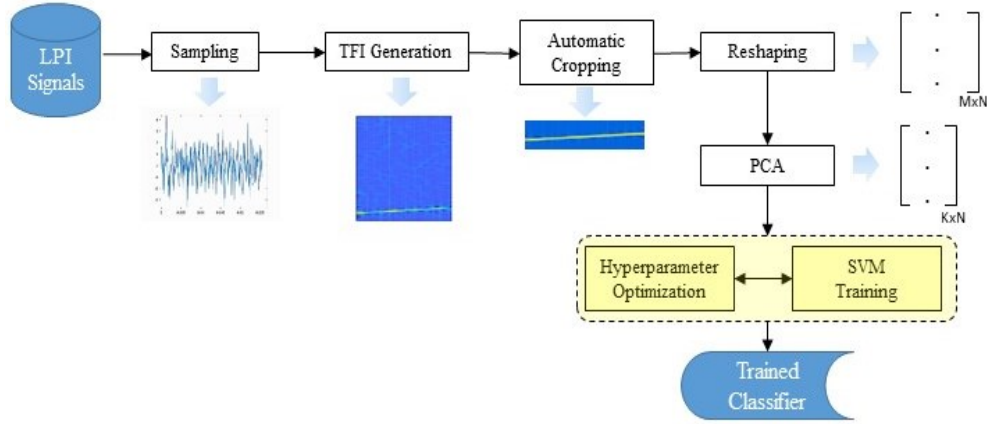


FIGURE 2. The flow diagram of the proposed LPI Radar Waveform classification technique.

Then, a hyperplane that creates the biggest margin m between points of both classes can be written as [16]:

$$y_i(x_i^T \beta + \beta_0) \geq m, \quad i = 1, \dots, N \quad (15)$$

In classification, the feature vectors of classes can be linearly-separable or not. For a non-linearly separable case, it is possible to create more flexible boundaries that minimize the amount of misclassified vectors. By designing a hyperplane classifier into a new k -dimensional space using the vectors which are the closest to the decision boundary, the non-linear case can also be classified. Mapping vectors into a high dimensional space provided by kernel operation.

It is stated that the computational complexity of SVM is independent of the dimensionality of the kernel space [17]. Thus, SVM can be used for a number of high dimensional models which make it a highly applicable algorithm. Since CWD creates a 3-dimensional TFI, the independence of computational complexity from the dimensions has become advantageous for the proposed technique.

Some of the commonly used Kernel functions (K_f) are described as:

$$d^{\text{th}}\text{-Degree polynomial: } K_f(x, x') = (1 + \langle x, x' \rangle)^d, \quad (16)$$

$$\text{Radial basis: } K_f(x, x') = \exp(-\gamma \|x - x'\|^2), \quad (17)$$

$$\text{Hyperbolic tangent [16]: } K_f(x, x') = \tanh(k_1 \langle x, x' \rangle + k_2) \quad (18)$$

There is no practical method to choose the best kernel function yet. It is also a challenging problem. For this purpose, No-Modulation signal and 12 LPI Radar signals are trained by SVM using 3 different kernel functions. Linear, 2nd order polynomial and Radial Basis Function are used as Kernel Function for classification. Then, different Kernel Functions are used for different signal types by using Hyper-Parameter Optimization.

During the training process, Hyper-Parameter optimization is applied. There may be multiple boundaries created by SVM that classifies the data. The most important parameters that characterize the boundary are penalty factor and Kernel parameters. By using these parameters, dozens of boundaries can be created that give correct classification. Finding the boundary that provides the most effectivity with minimum error is the objective of the SVM algorithm. Therefore, it becomes necessary to optimize the penalty factor and kernel parameters. These parameters are called Hyper-Parameters of SVM.

Bayesian Optimization [18] method is used for Hyper-Parameter Optimization. Bayesian Optimization is done by using a probabilistic model and an acquisition function. The probabilistic model is based on the observations that were made previously. The probabilistic model gives primary knowledge to find the locations of potential Hyper-Parameters. Acquisition function is used by defining an exploration ratio after each iteration and program evaluates whether the next point is over-exploiting or not. Exploration ratio provides the balance between exploring new points vs. concentrating near points. By exploring different points according to the given acquisition function, it results in a model.

As acquisition function, expected improvement (EI) plus is used.

$$E[I(\lambda)] = (f_{min} - \mu(\gamma))\Phi\left(\frac{f_{min} - \mu(\gamma)}{\sigma}\right) + \sigma\phi\left(\frac{f_{min} - \mu(\gamma)}{\sigma}\right) \quad (19)$$

where γ is a model of predictions which follows the normal distribution, $\Phi(*)$ is standard normal distribution function and $\phi(*)$ is standard normal density function and f_{min} is the best-observed value so far [19].

The blue points in Figure 3 show the explored Hyper-Parameter values with respect to estimated objective function values. As it can be understood from the model, the parameters with the highest estimated objective function values are the optimal Hyper-Parameters.

As a conclusion, the best scenario for SVM is created by optimizing parameters and using different Kernel functions.

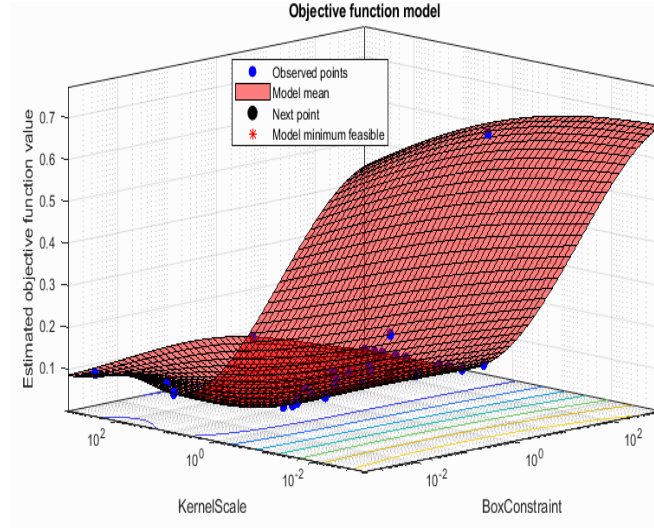


FIGURE 3. The exploration of objective function vs. SVM parameters during Hyper-Parameter Optimization

However, SVM is a classifier that requires high computational cost for the training process. In order to reduce the computational cost, principal components of the data matrix are obtained by computing the eigenvalues and eigenvectors. Then, K_e largest eigenvalues are chosen to form a transformation matrix \mathbf{A} that contains eigenvectors. Each $1 \times M$ ($=1 \times 12288$) dimensional feature vector \mathbf{x} transformed into a new $1 \times K_e$ dimensional vector \mathbf{y} that carries most of the information [20]. It can be calculated by

$$\mathbf{y} = \mathbf{A}^T \mathbf{x} \quad (20)$$

The correlation matrix S_y is determined by using (32)

$$S_y = E[\mathbf{y}\mathbf{y}^T] = E[\mathbf{A}^T \mathbf{x}\mathbf{x}^T \mathbf{A}] = \mathbf{A}^T S_x \mathbf{A} \quad (21)$$

where S is the diagonal matrix of eigenvalues. $E [^*]$ indicates the expected value of * .

By using the mean square error approximation, the K_e value can be specified for given conditions.

$$x = \sum_{i=0}^{M-1} y(i)a_i \text{ and } x' = \sum_{i=0}^{K_e-1} y(i)a_i.$$

Representing x by using x' gives a mean square error of

$$E [\|x - x'\|^2] = E \left[\left\| \sum_{i=K_e}^{M-1} y(i)a_i \right\|^2 \right] \tag{22}$$

By eigenvector definition, the mean square error is determined using

$$\sum_{i=K_e}^{M-1} a_i^T E [xx^T] a_i = \sum_{i=K_e}^{M-1} \lambda_i \tag{23}$$

As a result, to specify a K_e for a given mean square error can be determined by (23), [17].

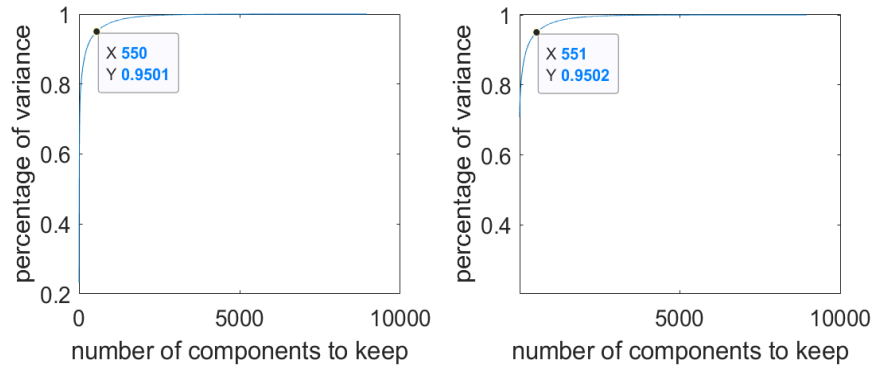


FIGURE 4. Percentage of variance vs. number of components to keep graph for PCA.

In the proposed technique, the mean square error of 5% is used where the percentage of variance becomes smaller than 0.01%. The result of the change of percentage of variance value is shown in Figure 4. A trial and error process is applied to set a mean square error value. In fact, the mean squared error value can be increased with a very little amount of information loss. Also, it results in a considerable reduction in the data load. However, trying to reduce the data load with different mean squared error values which are greater than 5% result in a performance loss in classification. As can be seen in Figure 4, from a certain point, the change in the percentage of variance becomes much smaller than before, meaning that from this point, features after K^{th} feature will make minor differences in classification.

By using PCA, around 550 of 12288 features are kept for one-against-all classification, around 130 of 12288 for one-against-one classification to represent 95% of each feature vector. The computational cost problem of SVM is reduced depending on PCA. The dataset with principal components makes the SVM an appropriate classification algorithm for LPI Radar waveform classification.

Since there are $C=13$ classes, it is needed to train $C*(C-1)/2 = 78$ binary SVMs. These SVMs are used to construct DDAG.

5. RESULTS

In the proposed technique, one-against-one and one-against-all methods are applied. For the one-against-one method, DDAG is used to find the best class. DDAG structure is given in Figure 5. The Confusion Matrix of the one-against-one method is shown in Table 6. For the one-against-all method, the maximum score-values of 13 SVMs are used to find the best class. The Confusion Matrix of the one-against-all method is shown in Table 5.

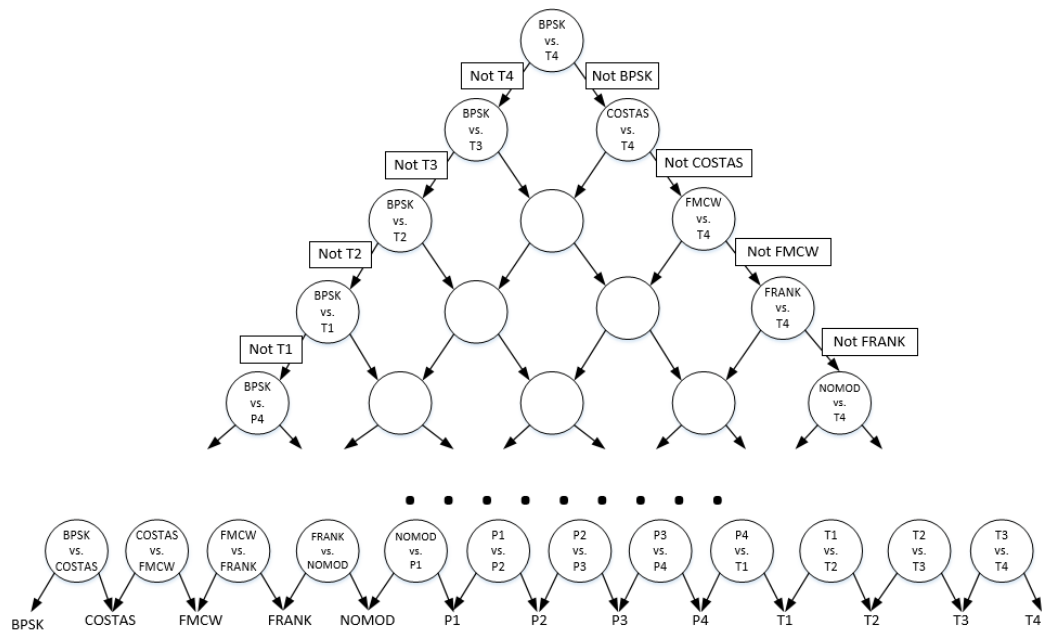


FIGURE 5. The Decision Directed Acyclic Graph for finding the best class out of 13 classes. (Not all of the nodes has been shown for the sake of clarity).

In addition, there are 4 important parameters that qualify the classification performance. *Accuracy*, *recall*, *precision* and *F-measure*. *Accuracy*, i.e. classification rate can be calculated by [21]:

$$\text{Overall Accuracy} = \frac{TP+TN}{TP+TN+FP+FN} \quad (24)$$

Where TP is the correctly classified feature vectors with label +1, FP is the misclassified feature vectors with label +1 and TN is the correctly classified feature vectors with label -1, FN is the misclassified feature vectors with label -1.

The *overall accuracy* of the one-against-all method is 98.73%. The poly-phase signals especially P1 and P4 are misclassified in between. The results of binary classification and multi-class classification are similar; the *overall accuracy* of the one-against-one method is 98.61%.

The *recall* is the ratio of the total number of correctly classified vectors of the class with label +1 and all vectors of the class with label +1. The *recall* value closer to 1 shows that the class with label +1 is correctly classified.

For a given feature vector labelled as +1, the *precision* gives the percentage that the given vector is actually labelled as +1. *Precision* is given by [21]:

$$\text{Precision} = \frac{TP}{TP+FP} \quad (25)$$

F-Measure represents both the precision and recall by taking their harmonic mean to save the balance in between. *F-Measure* is given by [21]:

$$\text{F_Measure} = \frac{2 \times \text{Recall} \times \text{Precision}}{\text{Recall} + \text{Precision}} \quad (26)$$

Classification performance parameters of one-against-all and one-against-one methods are given in Table 1 and Table 2, respectively.

Table 1. Accuracy, Recall, Precision, F-Measure values for one-against-all method

Accuracy	0.98730
Recall	0.98989
Precision	0.99237
F-Measure	0.99113

Table 2. Accuracy, Recall, Precision, F-Measure values for one-against-one method

Accuracy	0.98610
----------	---------

Recall	0.98996
Precision	0.99174
F-Measure	0.99085

The *recall*, *precision* and *F-measure* values cannot be compared to existing methods because there are no such values presented in these articles.

Table 3. Classification accuracy value comparison with other proposed techniques

	Proposed Technique	[3]	[4]	[5]	[8]
BPSK	98.96%	99.00%	66.17%	98.00%	NC**
COSTAS	100%	99.00%	77.67%	99.00%	NC**
LFM	100%	94.00%	68.58%	99.00%	95.00%
FRANK	100%	89.00%	65.83%	NA	85.00%
P1	87.35%	86.00%		86.00%	85.00%
P2	98.8%	100%	68.08%	100%	95.00%
P3	96.69%	91.00%	64.5%	98.00%	85.00%
P4	84.55%	85.00%	*64.08%	91.00%	85.00%
T1	100%	97.00%	66.00%	84.00%	NC**
T2	100%	94.00%	94.50%	92.00%	NC**
T3	98.36%	95.00%	68.83%	91.00%	NC**
T4	96.72%	94.00%	NC**	99.00%	NC**
BFSK***	NC**	NC**	NC**	NC**	95.00%
No Modulation	99.12%	NC**	NC**	NC**	95.00%

*In [4], P3 signal is taken as two different signal objects and one of this part and P4 are considered as one class. The other part of the P3 signal is taken as class P3. ** NC: Not Considered. *** BFSK signal stands for Binary Frequency Shift Keying and used only in [8].

Results of the proposed solution and [3], [4], [5] and [8] are given in Table 3. Since the *precision* and *F-Measure* values are not given in any of these, the reliability of these accuracy values can be arguable. In [3] the Confusion Matrix is created by using the results that have SNR value of -6dB. But Table 4 and Table 5 show the classification performance of all the SNR values examined including -18 and -20dB. Lower SNR values have substantial effects on classification performance. All of the accuracy values except the Costas Signal are higher in the proposed solution with the effect of lower SNRs. Therefore, the performance of the proposed solution can be said to be better. There is an abrupt change of classification performance for SNR values smaller than -12dB. In our technique, by the application of PCA, the confusing elements of the images are also eliminated, so the classification performance at these SNR values are also higher.

[4] proposes a different technique to classify Frank, P1, P3 and P4 codes. The Confusion Matrix is created by using lower SNR values so the accuracy values are lower than other techniques. But the point where the abrupt change occurs that is mentioned earlier is -14dB in [4]. For lower SNR values, the results are similar to the results obtained from the solution that we propose. However, the precision and *F-Measure* values are not mentioned in [4] either, so the overall results cannot be compared properly.

LPI Radar waveform recognition technique that is proposed in [5] gives better results for P3 and P4 signals. For poly-time signals, especially for T1, T2 and T3, there are major differences in the accuracy. The results that we obtained are much higher than the results in [5]. Since the Frank signal is excluded in [5], the similarity with the other poly-phase codes are not examined in between.

[8] used higher SNR values and fewer signal types for classification. However, their classification results are lower. For P4 signal, the classification performance is very close to the result that we obtained. But the resolution of the result of [8] is lower than ours and 84,55% can also be rounded to 85,00%. So they can be assumed to be the same. Simulations have been performed on the computer having 3.7 GHz processor and 16 GB memory. The required time to train one SVM in the one-against-all method is 1838 seconds on average, including PCA and Hyper-Parameter Optimization. The required time to train one SVM in the one-against-one method is 328 seconds on average, including PCA and Hyper-Parameter Optimization.

6. CONCLUSIONS

In this paper, an automatic LPI Radar classification method has been performed using SVM and Principal Component Analysis. SVMs are trained using methods of one-against-all and one-against-one with DDAG. Up to the PCA step, all distinctive features have been preserved.

Table 4. Confusion Matrix of the one-against-all method.

		SVM RESULTS												
		BPSK	COSTAS	FMCW	FRANK	NOMOD	P1	P2	P3	P4	T1	T2	T3	T4
ACTUAL SIGNAL TYPE	BPSK	0.9896	0.0000	0.0000	0.0000	0.0083	0.0000	0.0000	0.0000	0.0000	0.0000	0.0000	0.0000	0.0000
	COSTAS	0.0000	1.0000	0.0000	0.0000	0.0000	0.0000	0.0000	0.0000	0.0000	0.0000	0.0000	0.0000	0.0000
	FMCW	0.0000	0.0000	1.0000	0.0000	0.0000	0.0000	0.0000	0.0000	0.0000	0.0000	0.0000	0.0000	0.0000
	FRANK	0.0000	0.0000	0.0000	1.0000	0.0000	0.0000	0.0000	0.0000	0.0000	0.0000	0.0000	0.0000	0.0000
	NOMOD*	0.0088	0.0000	0.0000	0.0000	0.9912	0.0000	0.0000	0.0000	0.0000	0.0000	0.0000	0.0000	0.0000
	P1	0.0000	0.0000	0.0000	0.0000	0.0000	0.8735	0.0158	0.0065	0.1011	0.0000	0.0031	0.0000	0.0000
	P2	0.0000	0.0000	0.0000	0.0000	0.0000	0.0031	0.9880	0.0029	0.0060	0.0000	0.0000	0.0000	0.0000
	P3	0.0000	0.0000	0.0000	0.0000	0.0000	0.0069	0.0232	0.9669	0.0029	0.0000	0.0000	0.0000	0.0000

P4	0.0000	0.0000	0.0000	0.0000	0.0000	0.1113	0.0191	0.0172	0.8455	0.0069	0.0000	0.0000	0.0000
T1	0.0000	0.0000	0.0000	0.0000	0.0000	0.0000	0.0000	0.0000	0.0000	1.0000	0.0000	0.0000	0.0000
T2	0.0000	0.0000	0.0000	0.0000	0.0000	0.0000	0.0000	0.0000	0.0000	0.0000	1.0000	0.0000	0.0000
T3	0.0000	0.0000	0.0000	0.0000	0.0000	0.0000	0.0000	0.0000	0.0035	0.0000	0.0000	0.9836	0.0129
T4	0.0000	0.0000	0.0000	0.0000	0.0000	0.0000	0.0000	0.0000	0.0000	0.0000	0.0000	0.0328	0.9672

*NOMOD abbreviation is used instead of No-Modulation signal for the sake of simplicity.

Contrary to previous studies, operations such as averaging and converting to grey level are avoided. The Hyper-Parameters of SVMs has been optimized including kernel type by using Bayesian Optimization. The performances of methods have been obtained through simulations using different SNR levels. The overall accuracy level of 98.60% has been obtained from one-against-one and 98.73% has been obtained from the one-against-all method. The measure of classification performance is evaluated by calculating *F-measures*. It is observed that the classification performances are satisfactory compared to existing methods, except for -18 dB and -20 dB SNR values.

For low SNR values, the accuracy levels are also low for existing methods. The computational complexity of the method is enough for real-world ESM applications since the number of feature vectors is reduced using SVD. It can be concluded that the confused waveform cannot be considered as a big problem since the main objective of the LPI classification is to assign the jamming method against the LPI Radar, and similar jamming methods can be applied to confused LPI waveforms.

TABLE 5. *Confusion Matrix of the one-against-one method.*

		SVM RESULTS												
		BPSK	COSTAS	FMCW	FRANK	NOMOD	P1	P2	P3	P4	T1	T2	T3	T4
ACTUAL SIGNAL TYPE	BPSK	0.9969	0.0000	0.0000	0.0000	0.0083	0.0000	0.0000	0.0000	0.0000	0.0000	0.0000	0.0021	0.0000
	COSTAS	0.0000	1.0000	0.0000	0.0000	0.0000	0.0000	0.0000	0.0000	0.0000	0.0000	0.0000	0.0000	0.0000
	FMCW	0.0000	0.0000	1.0000	0.0000	0.0000	0.0000	0.0000	0.0000	0.0000	0.0000	0.0000	0.0000	0.0000
	FRANK	0.0000	0.0000	0.0000	1.0000	0.0000	0.0000	0.0000	0.0000	0.0000	0.0000	0.0000	0.0000	0.0000
	NOMOD	0.0055	0.0000	0.0000	0.0000	0.9945	0.0000	0.0000	0.0000	0.0000	0.0000	0.0000	0.0000	0.0000
	P1	0.0000	0.0000	0.0000	0.0000	0.0000	0.8438	0.0250	0.0063	0.1250	0.0000	0.0000	0.0000	0.0000
	P2	0.0000	0.0000	0.0000	0.0000	0.0000	0.0063	0.9625	0.0281	0.0031	0.0000	0.0000	0.0000	0.0000
	P3	0.0000	0.0000	0.0000	0.0000	0.0000	0.0063	0.0469	0.9438	0.0031	0.0000	0.0000	0.0000	0.0000
	P4	0.0000	0.0000	0.0000	0.0000	0.0000	0.1063	0.0219	0.0188	0.8531	0.0000	0.0000	0.0000	0.0000
	T1	0.0000	0.0000	0.0000	0.0000	0.0000	0.0000	0.0000	0.0000	0.0000	1.0000	0.0000	0.0000	0.0000
	T2	0.0000	0.0000	0.0000	0.0031	0.0000	0.0000	0.0000	0.0000	0.0000	0.0000	0.9969	0.0000	0.0000
	T3	0.0000	0.0000	0.0000	0.0000	0.0000	0.0000	0.0000	0.0000	0.0000	0.0000	0.0000	0.9688	0.0313
	T4	0.0000	0.0000	0.0000	0.0000	0.0000	0.0000	0.0000	0.0000	0.0000	0.0000	0.0000	0.0250	0.9750

REFERENCES

- [1] Pace, P.E., *Detecting and Classifying Low Probability of Intercept Radar*. 2nd Ed., Artech House, Norwood, MA, USA, 2009.
- [2] Tao, R., Li, B., Sun, H., Research Progress of the Algebraic and Geometric Signal Processing, *Defence Technology*, 9(1) (2013), 40-47.
- [3] Kong, S.H., Kim, M., Hoang, L.M., Kim, E., Automatic LPI Radar Waveform Recognition Using CNN, *IEEE Access*, 6 (2018), 4207-4219.
- [4] Hoang, L.M., Kim, M., Kong, S.H., Automatic Recognition of General LPI Radar Waveform Using SSD and Supplementary Classifier, *IEEE Transactions on Signal Processing*, 67(13) 2019, 3516-3530.
- [5] Gao, L., Zhang, X., Gao, J., You, S., Fusion Image Based Radar Signal Feature Extraction and Modulation Recognition, *Access IEEE*, 7 (2019), 13135-13148.
- [6] Huang, Z., Ma, Z., Huang, G., Radar Waveform Recognition Based on Multiple Autocorrelation Images, *Access IEEE*, 7 (2019), 98653-98668.
- [7] Gulum, T., Autonomous Non-Linear Classification of LPI Radar Signal Modulations, <https://calhoun.nps.edu/handle/10945/3302>; 2007 [accessed 24 September 2019].
- [8] Kishore, T.R., Rao, K.D., Automatic intrapulse modulation classification of advanced LPI radar waveforms, *IEEE Trans. Aerosp. Electron. Syst.*, 53(2) (2017), 901-914.
- [9] Tong, X., Modelling and realization of real time electronic countermeasure simulation system based on SystemVue, *Defence Technology*, 2019.
- [10] Deng, B., Luan, J., Cui, S., Analysis of parameter estimation using the sampling-type algorithm of discrete fractional Fourier transform, *Defence Technology*, 10(4) (2014), 321-327.
- [11] Liu, M., Liao, G., Yang, Z., Song, H., Gong, F., Electromagnetic Signal Classification Based on Deep Sparse Capsule Networks, *Access IEEE*, 7 (2019), 83974-83983.
- [12] Zeng, X., Wang, S., Bark-wavelet Analysis and Hilbert–Huang Transform for Underwater Target Recognition, *Defence Technology*, 9(2) (2013), 115-120.
- [13] Choi, H.I., Williams, W.J., Improved time-frequency representation of multicomponent signals using exponential kernels, *IEEE Trans. Acoust., Speech, Signal Process.*, 37(6) (1989), 862-871.
- [14] Hollinger, K.B., Code optimization for the Choi-Williams distribution for ELINT applications, <https://calhoun.nps.edu/handle/10945/4422>; 2009 [accessed 24 September 2019].
- [15] Liu, Y., Xiao, P., Wu, H., Xiao, W., LPI radar signal detection based on radial integration of Choi-Williams time-frequency image, *Journal of Systems Engineering and Electronics*, (2015), 973-981.
- [16] Hastie, T., Tibshirani, R., Friedman, J., *The Elements of Statistical Learning*, 2nd Ed., Springer New York Inc, New York, NY, USA, 2001.
- [17] Theodoridis, S., Koutroumbas, K., *Pattern Recognition*, 4th Ed., Academic Press. Inc., Orlando, FL, USA, 2009.
- [18] Snoek, J., Larochelle, H., Adams, R.P., Practical Bayesian optimization of machine learning algorithms, *Advances in Neural Information Processing Systems*, 25 (2012), 2960-2968.

- [19] Feurer, M., Hutter, F., Hyperparameter Optimization. In: Hutter F, Kotthoff L, Vanschoren, J., editors, Automated Machine Learning, Cham: Springer International Publishing, (2019), 3-33.
- [20] Duda, R.O., Hart, P.E., Stork, D.G., Pattern Classification, 2nd Ed., John Wiley & Sons, Inc. New York, 2001.
- [21] Powers, D.M.W., Evaluation: From Precision, Recall and F-Measure to Roc, Informedness, Markedness & Correlation, *Journal of Machine Learning Technologies*, 2(1) (2011), 37-63.
- [22] Lima, A.F., Analysis of low probability of intercept (LPI) radar signals using cyclostationary processing, <https://calhoun.nps.edu/handle/10945/4944>, 2002 [accessed 24 December 2019].
- [23] Platt, J. C., Cristianini, N., Shawe-Taylor, J., Large margin DAGs for multiclass classification, *Advances in Neural Information Processing Systems*, MIT Press, 12 (2000), 547–553.

MODERN LEARNING TECHNIQUES AND PLANT IMAGE CLASSIFICATION

Metehan UNAL, Erkan BOSTANCI, Mehmet Serdar GUZEL,
and Ayhan AYDIN

Ankara University, Department of Computer Engineering, Ankara TURKEY


ABSTRACT. The intelligent machines concept is born in sci-fi scenarios. Today it seems to be we are much closer to realizing this idea than ever before. By imitating the human nervous system, machines can learn many things. This paper explains modern learning techniques like artificial neural networks, transfer learning. Later purposes an experiment to classify plant seedling images to test the transfer learning with two different CNN architectures. Although the architects were not actually created for this task, result were quite accurate for a different classification task.


1. INTRODUCTION

The idea of “machines that can think” has emerged in the late 19th century in books as science-fiction scenario. After that, because of the world wars technology began to advance more rapidly than ever before. This progress has removed the obstacles to the realization of the concept of intelligent machines, which was previously only a sci-fi scenario.

In 1950, famous mathematician, computer scientist and crypto-analyst Alan Turing asked the question of “Can machines think?” [1]. This article can be considered as the beginning of the concept of Artificial Intelligence. In the same article, Turing introduced The Imitation Game, also known as the Turing Test. In this test, the machine, together with a person, is hiding outside the field of view of a person asking the questions. The interrogator tries to determine which is human and which is computer by asking questions. If the interrogator fails to correctly identify the person after a series of questions, the machine will pass the Turing test.

Keyword and phrases. Plan classification, convolutional neural network, AlexNet, VGGNet

 metehan.unal@ankara.edu.tr-Corresponding author; ebostanci@ankara.edu.tr; mguzel@ankara.edu.tr; ayaydin@ankara.edu.tr

 0000-0002-7545-2445; 0000-0001-8547-7569; 0000-0002-3408-0083; 0000-0001-7938-0509

Artificial Intelligence can be defined as the ability of a computer or a computer-controlled robot to perform various activities in the same way as intelligent living things [2]. In the years when the concept of Artificial Intelligence first emerged, researchers developed step-by-step methods that mimic the humans for solutions to the problems. Later, these methods were found to be insufficient on large data and more sophisticated methods were developed over the years. One of the most important of these modern methods is Machine Learning.

Machine learning is a field of study that aims to make software applications more accurate in predicting results without explicit programming. Machine learning is based on building algorithms that can predict outputs by statistical analysis, based on input data, and update outputs as new inputs arrive. Machine Learning algorithms generally examined into two categories as supervised and unsupervised algorithms.

Supervised algorithms required output data to test the results and generally applied on classification and regression problems. On the other hand, unsupervised algorithms do not require any output data and generally utilized to solve clustering problems.

In the last 10 years Deep Learning has emerged as a branch of Machine Learning. Deep Learning is a subset of Artificial Intelligence and Machine Learning, which predicts solutions to problems through experience using multi-layered artificial neural networks. Deep Learning differs from traditional methods in that it can automatically learn how data is represented without requiring expert or explicit coding.

Traditional machine learning techniques are limited by their ability to process natural data in raw forms. For many years, pattern recognition and machine learning systems required careful engineering and expertise to design feature extractors. Deep learning has enabled systems that do not require feature extraction.

Plants are very clearly one of the most important factors for the maintenance of natural life. Therefore, analysis, classification and protection of plants is a very important issue. Systems for classification and monitoring of plants have been developed in many parts of the world. Classification of plants by modern learning techniques, not by hand, will allow the systems to operate autonomously.

In this paper, first Artificial Neural Networks and Convolutional Neural Networks (CNN) were explained. Also two well-known CNN architectures were examined and Transfer Learning was explicated. After that, these two architectures were used to

classify a plan seedlings data set. In the last section, classification results were evaluated.

2. MODERN LEARNING TECHNIQUES

In this section, the details of Deep Learning techniques will be examined with the subtitles of Artificial Neural Networks, Convolutional Neural Networks and Architectures and Transfer Learning.

2.1. ARTIFICIAL NEURAL NETWORKS

Artificial Neural Networks are abstract structures that imitate the nervous system of people in order to develop robots that can learn like humans. The term neural is derived from the neuron, the basic functional unit found in the brain of the human nervous system.

Here, the concept of learning consists of adjusting the weights to decide the strength of the incoming signals.

In fact, the history of Artificial Neural Networks dates back to 1943. McCulloch and Pitts [3] developed a simple electrical circuit to model the neuron in their study. In the 1960s, perceptron which is the simplest neural network with a single cell, was developed for classification purposes. Perceptron failed to learn the XOR operation, while yielding pretty good results for AND and OR operations. This failure caused a loss of excitement and confidence over the field.

Until the beginning of the 21st century, interest in artificial neural networks increased and decreased periodically. In recent years, with the rapid development of graphic processing units of computers which enables huge amount of parallel processing power, the interest in artificial neural networks has reached the highest level.

2.2. CONVOLUTIONAL NEURAL NETWORKS

Convolutional Neural Networks is a type of multilayer perceptron. The structure of CNNs differs from that of other artificial neural networks (Fig. 1). Normal neural networks transform the input by inserting it into a series of hidden layers and each layer fully connected to the previous layer. In CNNs, the layers are primarily 3-dimensional, including depth, width and height. Not all neurons are fully connected

to each other, but only those in a certain region are interconnected. Furthermore, the output layer is a vector which includes probabilities.

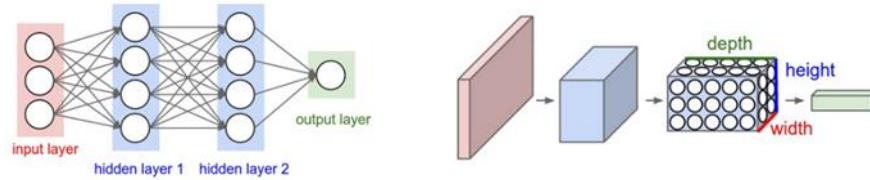


FIGURE 1. Normal Neural Network and Convolutional Neural Network [4].

CNN layers are divided into two parts which are feature extraction and classification. In the feature extraction part which is also named Hidden Layers, a series of convolution and pooling operations are performed. In the classification part which consist of fully-connected layers, classification is performed using extracted features.

2.3. CNN ARCHITECTURES

In this section the famous CNN architectures will be explained in detail. The architects to be mentioned here are those who succeed in the annual ImageNet face recognition competition [5]. In this competition, there is a data set of 1.2 million pictures and 1000 classes. This competition is held every year to find the architectures that classify this data set as the most successful.

The architecture that succeeded in this competition in 2012 is AlexNet [6]. AlexNet consists of a total of 8 layers with 5 convolutions and 3 fully-connected layers (Fig. 2). ReLU activation function and max pooling are used after each convolution layer. The ReLU activation function provides nonlinearity to the system.

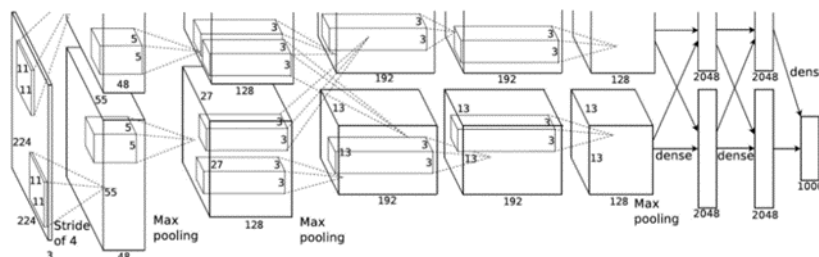


FIGURE 2. Architecture of AlexNet [6].

Another architecture is VGGNet [7], which produced successful results in the same competition in 2014. The number of layers of the VGGNet is 16 (Fig. 3), but there are versions with 19 layers. As it is understood, it has a much deeper structure than AlexNet. It has produced far more successful results than AlexNet by reducing the error rate from 16% to 8%.

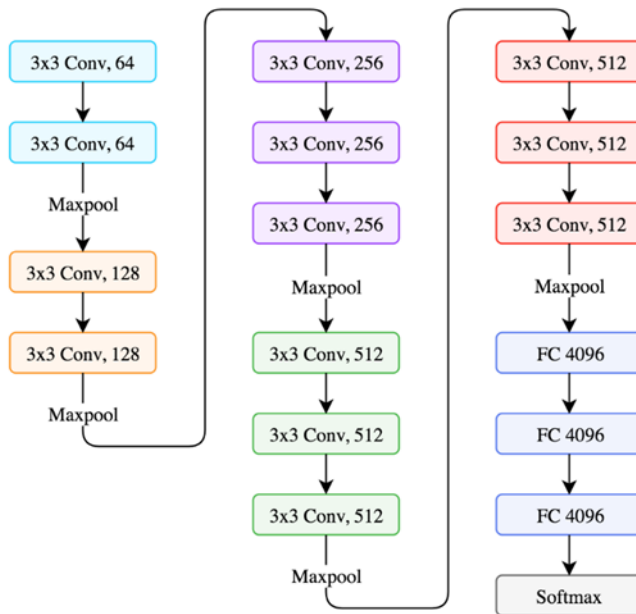


FIGURE 3. Architecture of VGGNet [7].

2.4. TRANSFER LEARNING

In practice, very few people try to create an artificial neural network from scratch, train it and calculate their weight. A network that has previously been trained for a

task can be used in other similar tasks. For this purpose, it is compulsory to remove the fully connected layers at the end of the artificial network. After removing the fully connected layers, a classifier based on the new problem which is working on, must be added. The remainder of the network is used as a feature extractor for the new dataset.

3. PLANT CLASSIFICATION

Plants have a very important place in natural life. Many countries around the world are forming plant monitoring networks in their regions. Therefore, plant identification and classification has become an important problem in recent years [9].

In plant classification problem, feature extraction method is used in the literature in general. For this purpose, classification procedures are made by looking at leaf shape [10-12], shape and surface [13], color [14] and vascular structure [15].

Larese et al. [16] classified vascular structures of bean leaves with Random Forest and SVM in their study and achieved successful results in the range of 87% to 95%. Grinblat et al. [17] improved previous work using a 5-layer CNN (Fig. 4) and increased the success range from 93% to 97%.

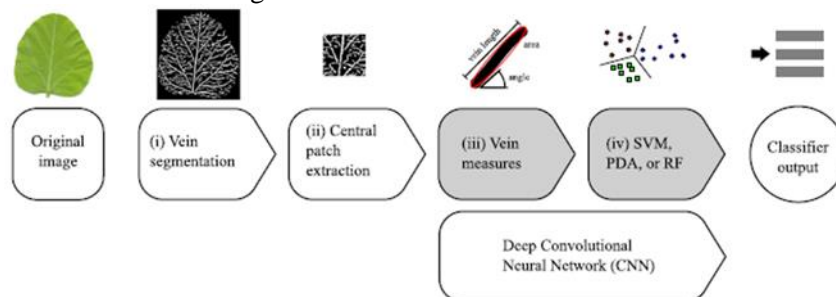


FIGURE 4. The system of the study of Grinblat et al. [17].

Lee et al. [18] used AlexNet architecture, a pre-trained model for object recognition. The artificial neural network architectures which was originally constructed for object recognition, can be used for other generic tasks and they produce very successful results [19]. As a result, they have achieved 99% success in the classification of the data set with 44 species of plant leaves.

3.1. EXPERIMENT

In this study we designed an experiment for plant classification using transfer learning method. The aforementioned AlexNet and VGGNet architectures were used for classification purposes. As stated before these two architecture were originally designed to classify faces but can be used for similar task like classification of plant pictures.

The experiment was conducted using Plant Seedlings [20] dataset of Aarhus University. This data set contains 4750. Sample images from data set can be seen in Fig. 5.

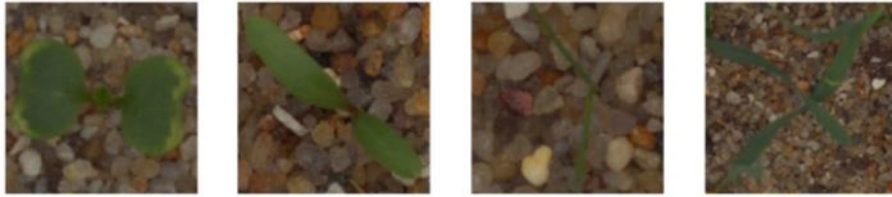


FIGURE 5. Sample images from dataset.

The specifications of the computer used in these experiments have Intel i7 7700K 4.20 Ghz CPU, Nvidia GeForce 1080 GPU, 16 GB RAM.

3.2. RESULTS

Dataset was used to test both architectures with 10-fold cross validation. Result of the training process of the AlexNet architecture can be seen in Fig. 6. Also training and validation loos of the architecture is in the Fig. 7.

Result of the 10 run of the 10-fold cross validation can be seen in Table 1. AS can be seen, AlexNet architecture produced better results regarding VGGNet. While VGGNet correctly classified the 75% of the plant images, success rate of the AlexNet was nearly 90%. Also result of the t-Test can be seen in Table 2. Looking at the table, one can see that the results are statistically significant ($t_{Stat} \gg t_{Critical}$, $P=1.29622E-11 \ll 0.05$).

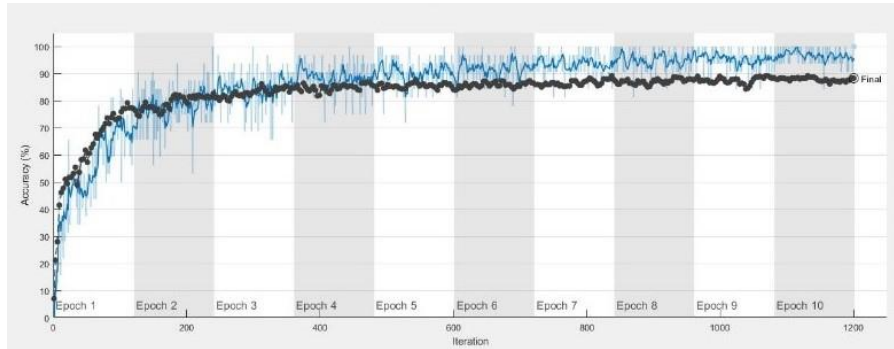


FIGURE 6. Result of the training process of the AlexNet architecture.

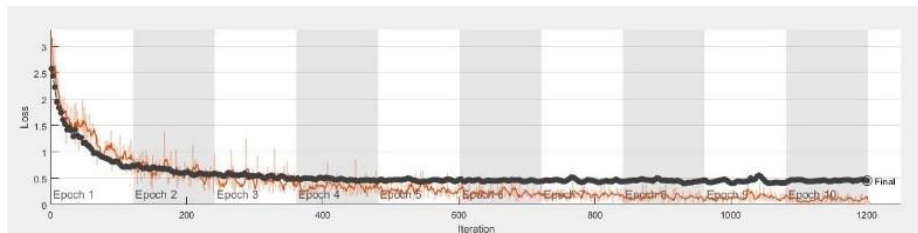


FIGURE 7. Sample training and validation loss.

TABLE 1. The results of 10 run of two different architectures.

	AlexNet	VGG16
1	0.8998	0.7589
2	0.8765	0.7554
3	0.8834	0.7640
4	0.8904	0.7585
5	0.8928	0.7491
6	0.8671	0.7434
7	0.8998	0.7569
8	0.8741	0.7446
9	0.8601	0.7475
10	0.8834	0.7510

TABLE 2. t-Test result.

	AlexNet	VGG16
Mean	0.88274	0.75293
Variance	1.79289E-03	4.65734E-05
Observations	10	10
Pearson Correlation	0.618046202	
Hypothesized Mean Difference	0	
df	9	
t Stat	38.63155235	
P(T<=t) one-tail	1.29622E-11	
t Critical one-tail	1.833112933	
P(T<=t) two tail	2.59244E-11	
t Critical two tail	2.262157163	

4. CONCLUSIONS

With the developing technology, machines became more and more intelligent day by day. The meaning of the intelligence in this context is the improvement of the ability to learn and to solve different problems. Since the very beginning of the artificial intelligence technology, scientists try to mimic human to enhance the learning ability. For this purpose, first perceptron was invented which followed by basic neural networks. After success of neural networks, deeper and more complex networks were generated to solve specific problems.

In this study, we designed a transfer learning method for plant image classification. First, artificial neural network and CNN was explained. Then different architectures of CNNs for modern face classification was mentioned. After that, transfer learning was explained. An experiment was evaluated for plant classification using this technique and a plant dataset.

The AlexNet architecture achieved better results than VGGNet on the dataset. The results show that a CNN architecture for a specific task can achieve good results in different tasks.

REFERENCES

- [1] Turing, A.M., Computing Machinery And Intelligence, *Mind*, Volume LIX, Issue 236, 1 October 1950, 433-460, <https://doi.org/10.1093/mind/LIX.236.433>.
- [2] Russell, S. J., Norvig, P. Artificial intelligence: a modern approach, Malaysia, Pearson Education Limited, 2016.
- [3] Zhang, L., Zhang, B. A geometrical representation of McCulloch-Pitts neural model and its applications, *IEEE Transactions on Neural Networks*, 10(4) (1999). 925-929.
- [4] Anonymous, Web Site: <http://cs231n.github.io/convolutional-networks/>, Access Date: 26.02.2017
- [5] Deng, J., Dong, W., Socher, R., Li, L. J., Li, K., Fei-Fei, L., Imagenet: A large-scale hierarchical image database, *IEEE conference on computer vision and pattern recognition, IEEE*, (2009, June), (pp. 248-255).
- [6] Krizhevsky, Alex, Sutskever, I., Geoffrey, E.H., Imagenet classification with deep convolutional neural networks, *Advances in neural information processing systems*, (2012).
- [7] Simonyan, K., Zisserman, A., Very deep convolutional networks for large-scale image recognition, arXiv preprint arXiv:1409.1556 (2014).
- [8] Yalcin, H., Razavi, S., Plant classification using convolutional neural networks, *Fifth International Conference on Agro-Geoinformatics (Agro-Geoinformatics), IEEE*, (2016, July), 1-5.
- [9] Chaki, J., Parekh, R., Designing an automated system for plant leaf recognition, *International Journal of Advances in Engineering & Technology*, 2(1) (2012), 149.
- [10] Gwo, C. Y., Wei, C. H., Li, Y., Rotary matching of edge features for leaf recognition, *Computers and electronics in agriculture*, 91 (2013), 124-134.
- [11] Arribas, J. I., Sánchez-Ferrero, G. V., Ruiz-Ruiz, G., Gómez-Gil, J., Leaf classification in sunflower crops by computer vision and neural networks, *Computers and Electronics in Agriculture*, 78(1) (2011), 9-18.
- [12] Husin, Z., Shakaff, A. Y. M., Aziz, A. H. A., Farook, R. S. M., Jaafar, M. N., Hashim, U., Harun, A., Embedded portable device for herb leaves recognition using image processing techniques and neural network algorithm, *Computers and Electronics in Agriculture*, 89 (2012), 18-29.
- [13] Ydipati, R., Burks, T. F., Lee, W. S., Identification of citrus disease using color texture features and discriminant analysis, *Computers and Electronics in Agriculture*, 52(1-2) (2006), 49-59.
- [14] Scoffoni, C., Rawls, M., McKown, A., Cochard, H., Sack, L., Decline of leaf hydraulic conductance with dehydration: relationship to leaf size and venation architecture, *Plant Physiology*, (2011), 111.
- [15] Larese, M. G., Baya, A. E., Craviotto, R. M., Arango, M. R., Gallo, C., & Granitto, P. M., Multiscale recognition of legume varieties based on leaf venation images, *Expert Systems with Applications*, 41(10) (2014), 4638-4647.

- [16] Grinblat, G. L., Uzal, L. C., Larese, M. G., Granitto, P. M., Deep learning for plant identification using vein morphological patterns, *Computers and Electronics in Agriculture*, (127) (2016), 418-424.
- [17] Lee, S. H., Chan, C. S., Wilkin, P., Remagnino, P., Deep-plant: Plant identification with convolutional neural networks, *IEEE International Conference on Image Processing (ICIP), IEEE*, (2015, September), 452-456.
- [18] Donahue, J., Jia, Y., Vinyals, O., Hoffman, J., Zhang, N., Tzeng, E., & Darrell, T. (2014, January). Decaf: A deep convolutional activation feature for generic visual recognition. *In International conference on machine learning* (pp. 647-655).
- [19] Giselsson, T. M., Jørgensen, R. N., Jensen, P. K., Dyrmann, M., Midtby, H. S., A public image database for benchmark of plant seedling classification algorithms, (2017), arXiv preprint arXiv:1711.05458.

A CONCATENATED UP AND DOWN TAPERED FIBER FOR SIMULTANEOUS MEASUREMENT OF STRAIN AND TEMPERATURE

Mustafa BILSEL and Isa NAVRUZ



Ankara University, Faculty of Engineering, Department of Electrical and Electronics
Engineering, Ankara, TURKEY

ABSTRACT. A novel fiber optical sensor based on in-line fiber Mach-Zehnder interferometer for simultaneous measurement of strain and temperature is proposed and demonstrated experimentally. The interferometer is simple, extremely robust and highly sensitive and consists of two concatenated parts; one is a down-tapered fiber (DTF) and the other is an up-tapered fiber (UTF). UTF and DTF sections of the sensor are fabricated by using a commercial fiber splicer and a non-commercial setup based on heating and stretching a portion of a standard single-mode fiber, respectively. While UTF section behaves as a beam splitter to decompose the injected light into core and cladding modes, DTF section provides evanescent field to access the surrounding environment. Experimental results indicate that the resolutions of 0.83 °C and 45.80 $\mu\epsilon$ were achieved in temperature and strain, respectively, for simultaneous measurement with a 10 pm of wavelength resolution.

1. INTRODUCTION

Simultaneous strain and temperature measurement ability of optical fiber sensors has attracted great attention in many research areas due to its importance in the fields such as environmental inspection, real-time structural health monitoring, tracing deformation in civil/mechanical engineering and aerospace industry. To satisfy distinct response to strain and temperature, these sensors usually include hybrid configurations or special type of fibers in their structure. Researchers have presented many techniques based on FBG, LPG, all-fiber Mach-Zehnder interferometer (MZI), special fiber assisted and their combinations. Recently, a broad range of devices and configurations have been investigated such as splicing FBG with multimode fiber and sandwiching them between two single mode fibers (SMFs) [1], combining FBG with a multimode fiber [2], splicing two FBGs written with different

Keyword and phrases. Up-tapered fiber, down-tapered fiber, simultaneous measurement, strain, temperature.

 mfbisel@gmail.com -Corresponding author; inavruz@ankara.edu.tr
 0000-0001-8252-3734;0000-0003-2976-076X

diameters [3], inscribing micro tapers on a slightly tapered fiber by using filament heating method [4], periodically micro-tapered fiber grating [5], using S tapered fiber embedded in FBG [6], cascading an LPG and a polarization maintaining fiber loop mirror [7] and combining an LPG with a high-birefringence fiber loop mirror [8]. Although these sensor structures accomplish adequate sensitivity in responding to strain and sensitivity, complex structure and fragility limit their use in potential applications. On the other side, special type of fiber-assisted MZIs have been fabricated such as an air-cavity embedded in a slightly tapered fiber via femtosecond laser [9], concatenating two up-taper fibers (UTF) [10], splicing a thin core fiber between two standard single-mode fibers and acting a core offset in one side of the thin core fiber [11], tapering a coreless multimode fiber as a sensing head [12] and Z-shape structure fabricated by exposing CO₂ laser on a single mode fiber [13]. However, their cost effectiveness is not satisfied owing to complicated fabrication and dependency on particular fiber type.

In this letter, we propose an all-fiber sensor formed by concatenating a UTF and a DTF joint. UTF structure was fabricated by using a commercial fusion splicer via splicing through setting the overlap parameter without changing the other splicing parameters. DTF structure was fabricated by using electrical arc discharge method in which a section of fiber was stretched while heating it up to its softening point so that diameters of both core and cladding decrease dramatically. In electrical arc discharge method, effective heat zone of electrodes is large so adiabaticity of DTF is adversely affected. For this reason, DTF sensors are required to be fabricated with small waist diameters to obtain a transmission spectrum with high fringe visibility. Practically, to get through the issue of thin waist diameter, UTF joint is a good choice and can impressively excite higher order cladding modes by satisfying the adiabaticity criteria. High-order cladding modes are generated when light interacts with UTF region because of the mismatch of the mode field diameter and it leads light to decompose into two parts, one propagating in the core and the other in the cladding of the fiber. Light confined between the taper region of DTF and surrounding medium can penetrate the surrounding environment in the form of evanescent wave. Changes in the conditions of the environment result in a wavelength shift in output interference spectrum as a function of surrounding parameters such as temperature, strain or refractive index.

2. SENSOR FABRICATION AND PRINCIPLE

Microscope captured images of the fabricated UTF and DTF are shown in Figure 1-(a) and (b), respectively. The proposed sensor structure is composed of two parts; leading UTF and subsequent DTF joint. Leading UTF is fabricated by using a commercial fiber splicer (Fujikura FSM-60s) in built-in mode by setting the overlap distance which is a measure of coincidence between two cleaved fiber ends when they pushed towards each other. To decompose fundamental mode into cladding modes and acquire interference spectrum with

desired free spectral range (FSR), maximum overlap distance of $150\ \mu\text{m}$ was chosen without changing the other splicing parameters. In splicing process, two stripped and cleaved fiber tips become softened and then push towards each other when electrodes are discharged so a gradually enlarged fiber diameter like a plump fiber is formed. Standard cladding diameter of $125\ \mu\text{m}$ was increased to about $165\ \mu\text{m}$. It generated an insertion loss of 9.6-12.7 dB when only UTF joint was applied to SMF. It means that about 90-95% of the total input power is coupled into cladding modes, 5-10% of optical power still remains propagating in the core mode.

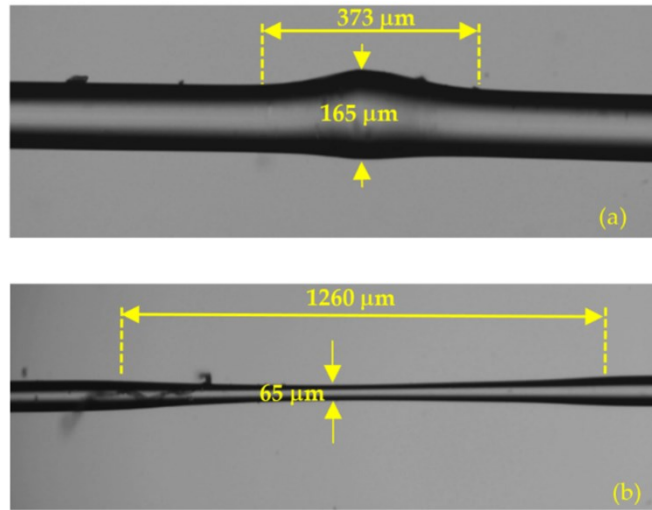


FIGURE 1. Microscopic image of (a) UTF and (b) DTF.

DTF joint of the proposed sensor was produced in our setup in Figure 2. We have also used the same setup in our experiments and it has also worked successfully to generate a DTF in our previous work [14]. Firstly, protective coating of a section of SMF was stripped and one end of the fiber was fixed with left fiber holder. The other end of the fiber is placed on right fiber holder whose motion is controlled by a stepper motor with a resolution of $1.25\ \mu\text{m}$ axial motion at each step. Secondly, a series of arc pulses are applied for a short time via electrodes to reach the softening point of the fiber and pulse duration is decreased to 80% of its maximum level. Then, steppers start to move in opposite direction; one stretching the fiber with a higher speed (stepper motor on the right) and the other moving the electrodes with a lower speed (stepper motor on the left). Acceleration and speed of fiber holders, pulse duration and instantaneous arc power are controlled by a computer software. Desired waist diameter and length of the taper can be adjusted by choosing suitable parameters in the

software. One of the major advantage of our setup compared to the commercial fusion splicer is no restriction on waist diameter and length. So, a tapered fiber section that one wishes to fabricate can be acquired with such a computer controlled setup. In the experiments, UTF joint has been initially fabricated, then DTF joint has been located at a distance of about 2 cm away from UTF. Wavelength spectrum is directly affected from the waist diameter so it is crucial to reproduce a sensor with the same geometry. To evaluate the reproducibility, 10 samples were fabricated with waist diameter of 65 μm and relative standard deviation was calculated as 1.8%. It is important to note that precise measurement of waist diameter from microscopic image also affects reproducibility.

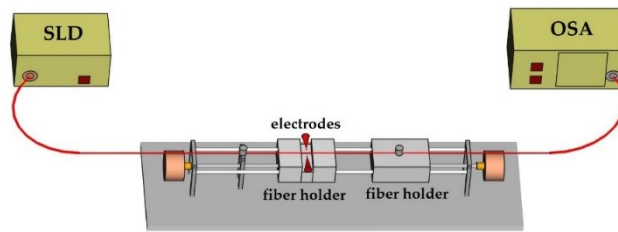
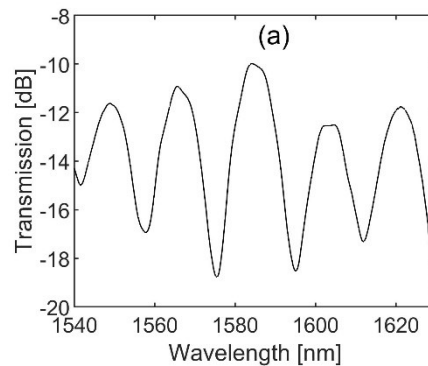


FIGURE 2. Experimental setup for fabrication of DTF.

At room temperature, typical transmission spectrum of the proposed sensor in air was shown in Figure 3-(a). Maximum extinction ratio for the dip located at 1575.5 nm is 8.7 dB. To investigate the cladding modes that contribute the interference spectrum, the Fourier transform was performed and the related spatial frequency spectrum was shown in Figure 3-(b). It indicates that only one cladding mode has been stimulated and contributed to the interference spectrum.



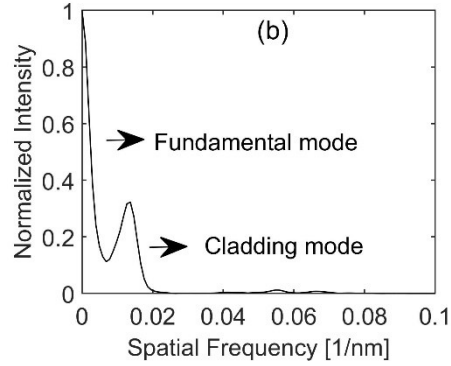


FIGURE 3. (a) Typical spectrum at room temperature in air and (b) its Fourier transform.

Assuming only one core mode is excited, then output intensity of MZI can be expressed as [15],

$$I = I_{co} + I_{cl} + 2\sqrt{I_{co}I_{cl}}\cos\varphi \quad (1)$$

where I is the intensity of throughput, I_{co} and I_{cl} are the intensities of core and cladding modes, respectively, and φ is the phase difference between core and cladding modes. Due to difference in refractive index of core and any cladding mode, a phase difference between them occurs:

$$\varphi = \frac{2\pi\Delta n_{eff}L}{\lambda} \quad (2)$$

where Δn_{eff} is the effective refractive index difference between core and cladding modes, L is the length of the sensor and λ is the wavelength of the light. When phase difference becomes equal to odd-multiple of π , that is, $\varphi = (2m+1)\pi$, where m is an integer, destructive interference occurs and dip points in interference spectrum is observed. Dip wavelength of the m -th order cladding mode in interference spectrum can be expressed as:

$$\lambda_{dip} = \frac{2\Delta n_{eff}L}{2m+1} \quad (3)$$

Differentiating Eq. (3) with respect to temperature, T , yields temperature dependency of dip wavelength:

$$\frac{\partial \lambda_{dip}}{\partial T} = \frac{2}{2m+1} \left[\Delta n_{eff} \frac{\partial L}{\partial T} + L \left(\frac{\partial n_{eff}^{co}}{\partial T} - \frac{\partial n_{eff}^{cl}}{\partial T} \right) \right] \quad (4)$$

where the first term in squared brackets, $\partial L/\partial T$, is thermal-expansion coefficient of silica which represents the variation of sensor length with temperature, and the second term, $\frac{\partial n_{eff}^{co}}{\partial T} - \frac{\partial n_{eff}^{cl}}{\partial T}$ is thermo-optical coefficient of silica which denotes the change in refractive index of both core and cladding with respect to temperature. For silica, thermal-expansion and thermo-optic coefficients are $0.55 \times 10^{-6} / ^\circ\text{C}$ and $8.0 \times 10^{-6} / ^\circ\text{C}$ [16], respectively, which means thermo-optic coefficient is the dominant term in the case of temperature variation. Similarly, response of dip wavelength to applied strain can be expressed as,

$$\frac{\partial \lambda_{dip}}{\partial \varepsilon} = \frac{2}{2m+1} \left[\Delta n_{eff} \frac{\partial L}{\partial \varepsilon} + L \left(\frac{\partial n_{eff}^{co}}{\partial \varepsilon} - \frac{\partial n_{eff}^{cl}}{\partial \varepsilon} \right) \right] \quad (5)$$

where ε is the applied strain. According to the equation, both length and refractive index of refraction are affected from strain due to elasto-optical effect. Strain can be defined as [17],

$$\varepsilon = \frac{\Delta L}{L} \quad (6)$$

where L is initial length and ΔL is the change in length.

Simultaneous measurement of strain and temperature can be investigated by monitoring wavelength shift of two dips. Coefficient matrix [11] which includes experimentally calculated sensitivities and wavelength shifts can be used to find the resolution of the sensor in simultaneous strain and temperature measurement:

$$\begin{bmatrix} \Delta \lambda_A \\ \Delta \lambda_B \end{bmatrix} = \begin{bmatrix} S_{T,A} & S_{\varepsilon,A} \\ S_{T,B} & S_{\varepsilon,B} \end{bmatrix} \begin{bmatrix} \Delta T \\ \Delta \varepsilon \end{bmatrix} \quad (7)$$

where $\Delta \lambda_A$ and $\Delta \lambda_B$ are the wavelength shifts; $S_{T,A}$, $S_{T,B}$ are temperature sensitivities; $S_{\varepsilon,A}$, $S_{\varepsilon,B}$ are strain sensitivities of dipA and dipB, respectively. ΔT and $\Delta \varepsilon$ are variations of ambient temperature and applied strain, respectively.

3. RESULTS AND DISCUSSION

To characterize the proposed MZI sensor, light from a superluminescent diode (SLD) source with a range of 1450-1650 nm was injected to the sensor and the interference spectrum was recorded by an optical spectrum analyzer (Thorlabs OSA-202) with a maximum resolution of 30 pm. For strain measurements, same setup in Figure 2 was used without operating electrodes, that is, when one end of the MZI was fixed with left fiber holder, the other end was clamped on right fiber holder. Each time right stepper was moved a particular distance an external force was acted on fiber. Referring to Figure 3-(a), the resonant dips named as

dipA, dipB and dipC located at 1575.5, 1595.2, 1611.8 nm were followed for strain and temperature measurements. Due to cross-sensitivity temperature was kept constant during strain measurements and vice versa. Transmission spectrum of the proposed sensor with different strain was shown in Fig. 4-(a). Resonant dips showed blue-shift when strain values were increased from 0 $\mu\epsilon$ to 1430 $\mu\epsilon$. To avoid possible errors in calculating sensitivity, it should be assured that dips do not include ripples. For this reason, enlarged views of all dips were plotted in Figure 5. According to the figure, total shift in dipA, dipB and dipC was 1.5 nm, 1.4 nm and 0.9 nm, respectively. Signal variation in dip points is due to type of cladding modes excited. It indicates that dipC is less sensitive to strain, thereby it is thought dipC is resulted from UTF joint. Variation of dip points with respect to applied strain was analyzed by linear fitting. The corresponding sensitivities of dipA, dipB and dipC to strain were calculated as 1.00 pm/ $\mu\epsilon$, 0.95 pm/ $\mu\epsilon$ and 0.69 pm/ $\mu\epsilon$, respectively as shown in Figure 4-(b). The correlation coefficient values (R^2) higher than 0.99 were achieved, which exhibited good linear response. Assuming an OSA with 10 pm wavelength resolution, the proposed sensor can achieve strain resolution of 9.90 $\mu\epsilon$ for dipA in discrete strain measurements.

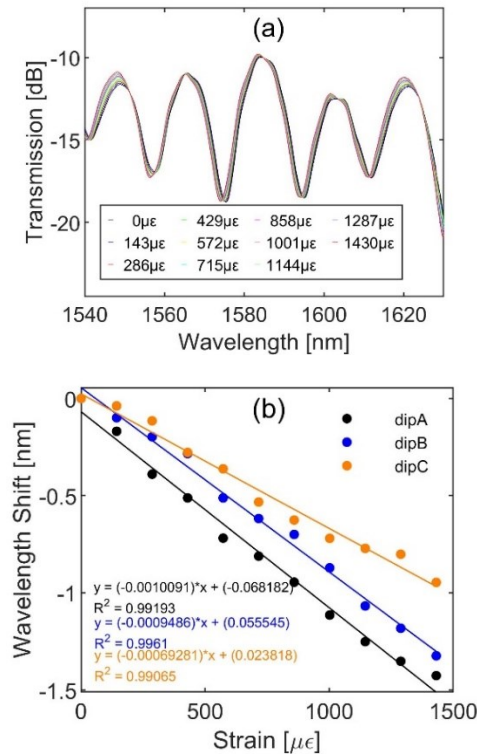


FIGURE 4. (a) Transmission spectrum with different strain and (b) wavelength shift of dip points versus tensile strain.

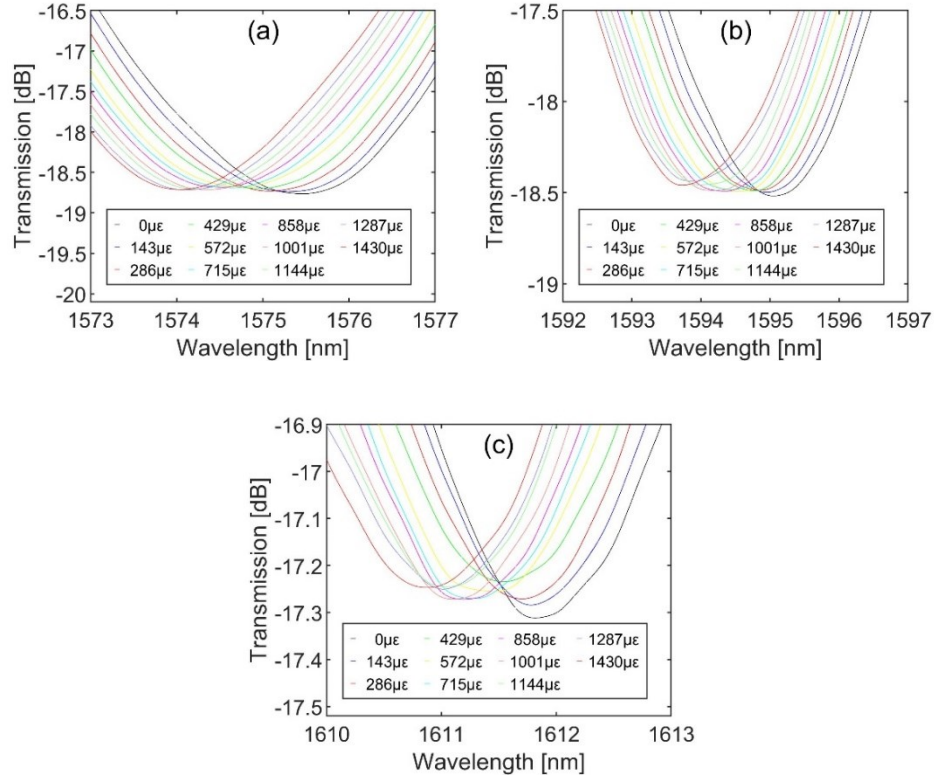


FIGURE 5. Enlarged views of (a) dipA, (b) dipB and (c) dipC.

In temperature measurements, a proportional-integral-derivative (PID) controlled furnace manufactured in our laboratory was used. Resistive element with power of 300 W was placed in the furnace and its power control was achieved with a commercial temperature controller (ENDA ETC4420). Inner temperature of the furnace can be set with an accuracy of ± 0.1 $^{\circ}\text{C}$ and the temperature was measured by a calibrated temperature probe (Testo 100) with a resolution of 0.1 $^{\circ}\text{C}$. To keep the strain constant during temperature measurements, sensor was flattened on an aluminium plate placed in the furnace. When temperature was increased in the range of 21-65 $^{\circ}\text{C}$, all the dips exhibited red-shift as shown in Figure 6-(a). According to the figure, dipC with total shift of 2.3 μm was experienced the highest response to temperature variation although its response to strain was low. This result verified the origin of dipC and we infer that it is due to the UTF joint. As shown in Figure 6-(b), temperature

sensitivities of 41.92 pm/°C, 40.01 pm/°C and 49.92 pm/°C were acquired for dipA, dipB and dipC, respectively. The correlation coefficient greater than 0.99 shows good linearity in measurements. Temperature resolution of 0.2 °C in discrete temperature measurements can be achieved by following dipC for 10 pm wavelength resolution.

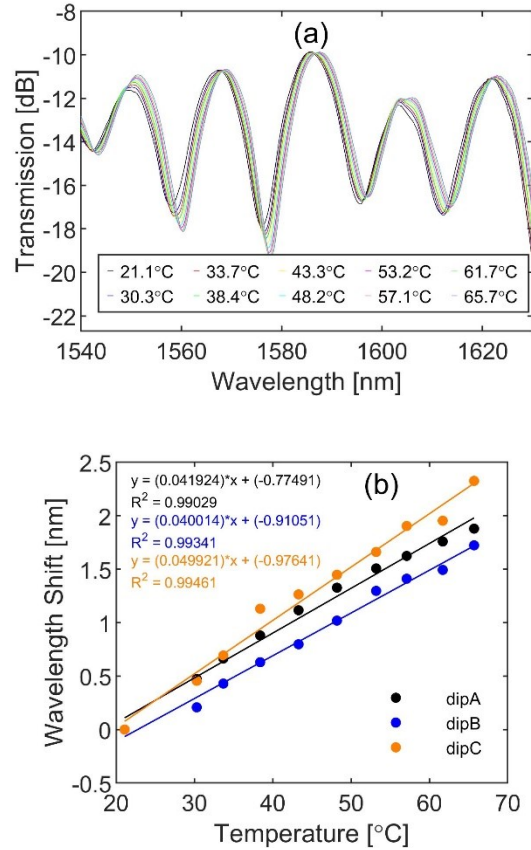


FIGURE 6. (a) Transmission spectrum with different temperature and (b) wavelength shift of dip points versus temperature.

Under the same experimental conditions, strain and temperature measurements repeated 3 times to investigate the repeatability. Resultant strain and temperature sensitivity plots for dipA were shown in Fig. 7.a and Fig. 7.b, respectively. Relative standard deviations in three measurements were calculated as 0.8% and 2.1% for strain and temperature, respectively. Calculations for dipB and dipC had similar results with dipA. It means that the proposed sensor has good repeatability.

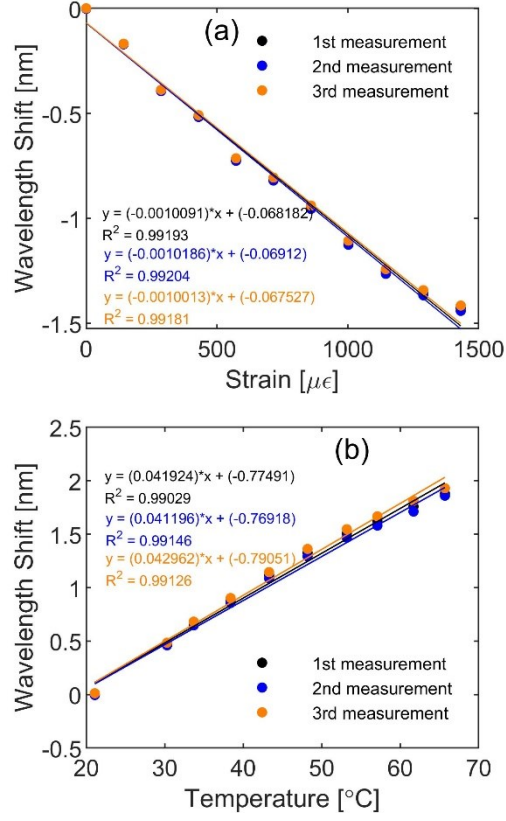


FIGURE 7. Reiterated experiments of (a) strain and (b) temperature.

By using sensitivity values obtained from experimental results, coefficient matrix introduced in Eq. 7 can be written to find the resolution of the proposed sensor for simultaneous measurement of strain and temperature:

$$\begin{bmatrix} \Delta\lambda_B \\ \Delta\lambda_C \end{bmatrix} = \begin{bmatrix} 40.014 & -0.9486 \\ 49.921 & -0.692 \end{bmatrix} \begin{bmatrix} \Delta T \\ \Delta\epsilon \end{bmatrix} \quad (8)$$

Assuming $\Delta\lambda_B = \Delta\lambda_C = 10$ pm for the wavelength resolution of OSA, resolution of the sensor was calculated as 0.83 °C and 45.80 μϵ for temperature and strain, respectively.

A comparison table was constructed to compare sensitivity of the proposed sensor with the sensors which can perform simultaneous measurement of strain and temperature. Table 1

reveals that proposed sensor exhibits higher sensitivity than Refs. [1, 2, 5, 18, 19] and Refs. [3, 6, 12, 18, 19, 20] in terms of strain and temperature, respectively, and almost the same characteristics with Ref. [10].

TABLE 1. Comparison of sensitivity.

Sensor [Ref]	Sensitivity ($\text{pm}/\mu\epsilon$)	Sensitivity ($\text{pm}/^\circ\text{C}$)
1	0.48	52.00
2	-0.84	-243.40
3	2.57	8.50
5	-0.55	49.60
6	54.97	14.71
10	1.03	57.50
12	-23.70	16.56
18	0.65	40.17
19	0.76	13.20
20	-1.86	9.70
Proposed sensor	1.00	49.92

However, Refs. [4, 9, 13] require expensive and complex equipments to fabricate the sensor and Refs. [7, 8, 16] involve special type fibers so these drawbacks limit their practical use. Consequently, proposed sensor is much easier to fabricate, less expensive, based on standard telecom fiber and needs easier experimental setup compared to dual-parameter sensors available in the literature.

4. CONCLUSION

An easy MZI concatenating a UTF and a DTF for simultaneous measurement of strain and temperature was investigated and demonstrated experimentally. Experimental results indicated that strain resolution of $9.9 \text{ pm}/\mu\epsilon$ and temperature resolution of $0.2 \text{ }^\circ\text{C}$ were achieved for discrete measurements. For simultaneous measurements, resolutions of $0.83 \text{ }^\circ\text{C}$ and $45.80 \mu\epsilon$ were calculated by using coefficient matrix for temperature and strain, respectively. The thinnest waist diameter is $65 \mu\text{m}$ so the interferometer is extremely robust. Besides, compactness of the interferometer is provided without including any splicing joint in sensor structure. The interferometer is all-fiber type, cost effective, simple to fabricate and provides high resolution, in that respect, it can be a good choice in simultaneous measurements of strain and temperature in extensive applications.

Acknowledgments. This research did not receive any specific grant from funding agencies in the public, commercial, or not-for-profit sectors. Also, the authors would like to thank Net System Infrastructure Services Co. for their support.

REFERENCES

- [1] Sun, H., Yang, S., Zhang, X., Yuan, L., Yang, Z., Hu, M., Simultaneous measurement of temperature and strain or temperature and curvature based on an optical fiber Mach-Zehnder interferometer, *Opt. Comm.*, 340 (2015), 39-43.
- [2] Zhou, D. P., Wei, L., Liu, W. K., Liu, Y., Lit, J. W. Y., Simultaneous measurement for strain and temperature using fiber Bragg gratings and multimode fibers, *App. Optics.*, 47 (2008) 1668-72.
- [3] Jiang, N., Zhu, H., Bao, K., Hu, Y., Simultaneous discrimination of strain and temperature using dual-gratings in one fiber, *Optik*, 126 (2015) 3974-7
- [4] Yang, W., Geng, T., Yang, J., Zhou, A., Zhaojun, L., Geng S., Yuan, L., A phase-shifted long period fiber grating based on filament heating method for simultaneous measurement of strain and temperature, *J. Opt.*, 17 (2015), 1-6.
- [5] Yoon, M. S., Park, S., Han, Y. G., 2012 Simultaneous measurement of strain and temperature by using a micro-tapered fiber grating, *J. Ligh. Tech.*, 30 (2011) 1156-60
- [6] Li, J., Yang, S., Zhang, W., Gao, S., Bai, Z., Wang, L., Liang, H., Yan, T., Simultaneous force and temperature measurement using S fiber taper in fiber Bragg grating, *IEEE Phot. Tech. Lett.*, 26 (2014), 309-312.
- [7] Chu, J., Shen, C., Qjan, F., Zhong, C., Zou, X., Dong, X., Jin, Y., Wang, J., Gong, Y., Jiang, T., Simultaneous measurement of strain and temperature based on a long-period grating with a polarization maintaining fiber in a loop mirror, *Opt. Fib. Tech.*, 20 (2014), 44-47.
- [8] Frazao, O., Marques, L. M., Santos, S., Baptista, J. M., Santos, J. L., Simultaneous measurement for strain and temperature based on a long-period grating combined with a high-birefringence fiber loop mirror, *IEEE Phot. Tech. Lett.*, 18 (2006), 2407-2409.
- [9] Chen, H. F., Wang, D. N., Wang, Y., Simultaneous strain and temperature sensing using a slightly tapered optical fiber with an inner cavity, *Analyst*, 140 (2015), 1859-1862.
- [10] Dong, B., Peng, Y., Wang, Y., Yu, C., Mode division multiplexing in a fiber modal interferometer for dual-parameters measurement, *IEEE Phot. Tech. Lett.*, 28 (2016), 143-146.
- [11] Zhou, J., Liao, C., Wang, Y., Yin, G., Zhong, X., Yang, K., Sun, B., Wang, G., Li, Z., Simultaneous measurement of strain and temperature by employing fiber Mach-Zehnder interferometer, *Opt. Exp.*, 22 (2014), 1680-1686.
- [12] Andre, R. M., Biazoli, C. R., Silva, S. O., Marques, M. B., Cordeiro, C. M. B., Frazao, O., Strain-temperature discrimination using multimode interference in tapered fiber, *IEEE Phot. Tech. Lett.*, 25 (2013), 155-158.

- [13] Zhang, C., Lu, P., Liao, H., Ni, W., Fu, X., Jiang, X., Liu, D., Zhang, J., Simultaneous measurement of axial strain and temperature based on a Z-Shape fiber structure, *IEEE Phot. J.*, 9 (2017), 1-9.
- [14] Navruz, I., Ari, F., Bilsel, M. and AL-Mashhadani, Z. A., Enhancing refractive index sensitivity using micro-tapered long-period fiber grating inscribed in biconical tapered fiber, *Opt. Fib. Tech.*, 45 (2018), 201-207.
- [15] Ghatak, A., *Optics* (4th Ed.), Tata McGraw-Hill, 2009.
- [16] Chen, L. X., Huang, X. G., Li, J. Y., Zhong, Z. B., Simultaneous measurement of refractive index and temperature by integrating an external Fabry-Perot cavity with a fiber Bragg grating, *Rev. Sci. Inst.*, 83 (2012), 053113.
- [17] Serway, R. A., Jewett, J. W., *Physics for Scientist and Engineers* (6th Ed.), Thomson Brooks/Cole, 2004.
- [18] Qi, T., Xiao, S., Shi, J., Zhou, Z., Bi, M., Li, P., Simultaneous strain and temperature measurement using compact core-offset inter-modal interferometer with embedded fiber Bragg grating, *Asia Communications and Photonics Conference ACP*, Guangzhou, China (2012).
- [19] Hu, Q., Wang, P., Rao, B., Wang, M., Wang, Z., Xu, X., Simultaneous measurement of temperature and strain using double-cladding fiber based hybrid Bragg grating, *OSA Cont.*, 4 (2020), 1031-1037.
- [20] Naeem, K., Chung, Y., Kim, H., Cascaded two-core PCFs-based in-line fiber interferometer for simultaneous measurement of dtrain and temperature, *IEEE Sensors J.*, 19 (2019), 3322-3327.

TOWARDS REAL TIME IMAGE DEHAZING ON ANDROID OPERATING SYSTEM

Yücel ÇİMTAY

HAVELSAN, Signal and Image Processing Group, Ankara, Turkey

ABSTRACT. Haze is one of the most important effects that degrades the quality of the image and video. This diminishes contrast and reduces visual efficiency. The atmospheric light scattering model (ALS) is commonly used for dehazing. There are two unknowns to be measured in this model: atmospheric light and transmission from scene. Such calculations are not easy, and the calculation of atmospheric light is very time consuming. This condition makes it difficult to dehaze in real time. Although dehazing applications have been applied widely for long time, this work is one of the first tries of real time dehazing on android operating system. This is very important in terms of transforming the real time dehazing to mobile platforms. According to the results, this study can run in near real time, and is able to go towards real time by using more powerful hardware.

1. INTRODUCTION

Image and video dehazing are crucial for offline and online computer vision applications needed in security, transportation, video surveillance and military areas. Consequently, the number of studies related to image enhancement has steadily increased in recent years [1]. Image dehazing is a kind of image enhancement, but it varies from others due to changes in image deterioration regarding the scene distance from the observation point and the amount of haze globally and locally. In other terms while the distance between sensor and scene is increasing the thickness of haze also increases and the transmission of media decreases. Similarly, when the density of haze is high and differs locally the complexity of dehazing process increases. To illustrate, Figure 1 displays two hazy and haze-free image pairs. Image (a) is a hazy

Keyword and phrases. Atmospheric light, hazy imagery, depth map, transmission

 yuclcimtay@gmail.com
 0000-0003-2980-9228

© 2020 Ankara University

Communications Faculty of Sciences University of Ankara Series A2-A3: Physical Sciences and Engineering

image, and (b) is the result of haze removal process applied to (a). Similarly, c is the hazy image and (d) is the haze-free pair of (c). It is obvious from the images that the thickness of haze is more in the second image pair. Therefore, haze removal is less effective, and the visual quality is lower.

There are many ways of image dehazing and they can be grouped in three categories which are (1) contrast enhancement [2-5], (2) restoration [6-10] and (3) fusion based [11-15] methods. Contrast enhancement approaches increase the visual image to some extent; however, they cannot fully eliminate the haze. The subcategories of image enhancement models are histogram enrichment which can be applied locally and/or globally, frequency transform methods: wavelet transform, and homomorphic filtering, and Retinex method: single and multi-scale Retinex [16]. Restoration based methods model the image degradation and applies inverse filtering. By this way the lost information is recovered.

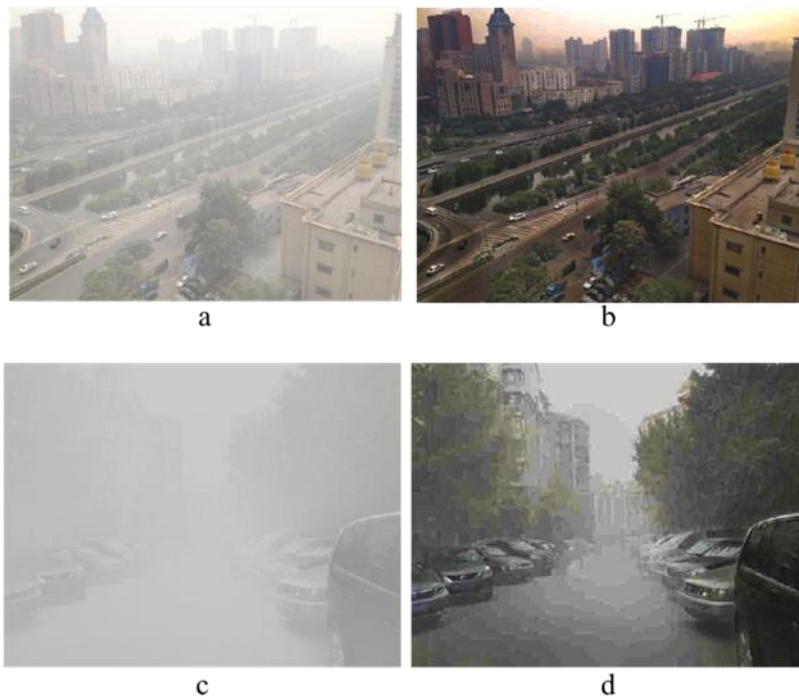


FIGURE 1. Hazy-haze free image pairs

Because this paper is based on the application of image dehazing in real time, we are not going into the specifics for these methods. On the other hand, as the basis

of our analysis, we are using the atmospheric light scattering model shown in Figure 2.

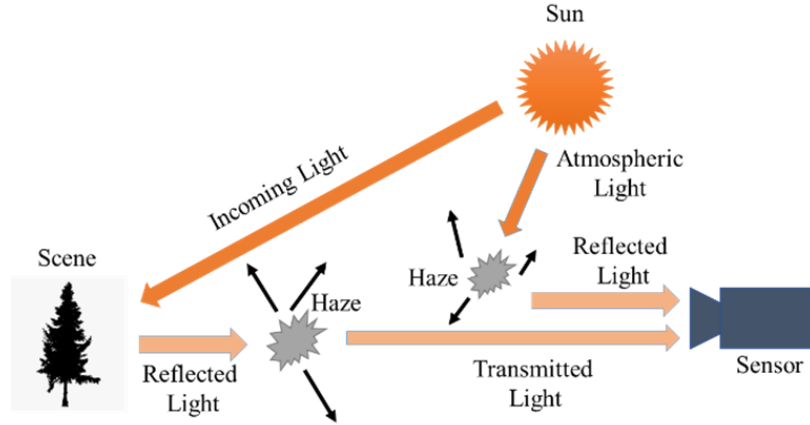


FIGURE 2. Atmospheric light scattering model

Equation 1.1-1.3 express atmospheric scattering model where $I(x, \lambda)$ is the hazy image, $D(x, \lambda)$ is transmitted light through haze (after the reflection from scene) and $A(x, \lambda)$ air light which is the reflected atmospheric light from haze. The sensor integrates the incoming lights and the resultant imagery is the hazy image. In Equation 1.2, $t(x, \lambda)$ is transmission of haze, $R(x, \lambda)$ is the reflected light from the scene and L_∞ is the atmospheric light. Transmission term is expressed as $e^{-\beta(\lambda)d(x)}R(x, \lambda)$ where $d(x)$ is the depth map of scene and $\beta(\lambda)$ is atmospheric scattering coefficient related to capturing wavelength. It can be easily understood from Equation 1.3 is that as the depth from the sensor increases, transmission decreases and vice versa.

$$I(x, \lambda) = D(x, \lambda) + A(x, \lambda) \quad (1.1)$$

$$= t(x, \lambda)R(x, \lambda) + L_\infty(1 - t(x, \lambda)) \quad (1.2)$$

$$= e^{-\beta(\lambda)d(x)}R(x, \lambda) + L_\infty(1 - e^{-\beta(\lambda)d(x)}) \quad (1.3)$$

The key point here is, the exact calculation of the term of transmission and atmospheric light. The Dark Channel Prior (DCP) Method [17] is one of the commonly used methods. In simple DCP, the per-pixel dark channel prior is used

for haze estimation. On the other hand, for measuring the atmospheric light, quadtree decomposition is applied. Another research that uses the DCP as its basis is [18]. In this study, both per-pixel and spatial blocks are used when calculating dark channel. Recent approaches on image dehazing is mostly based on artificial intelligence models like deep learning [19-21]. In [22] a deep architecture is developed by using Convolutional Neural Networks (CNN) and it adds a new unit to network called “bilateral rectified linear unit”. It reports that it achieves superior results compared to previous dehazing studies. The study in [23] employs an end-to-end encoder-decoder CNN architecture to handle haze free images.

There are many successful image dehazing studies in the literature. However, when the focus is real time application, there are always bottlenecks such as the complexity of algorithms, hardware constraints and high financial costs. Nonetheless, there have been several successful studies underway. The study in [24] estimates the atmospheric light by using super-pixel segmentation and applies guidance filter to refine the transmission map. This study mentions that it achieves more accurate results compared to other state of the art models. The study in [25] proposes parallel processing dehazing method for mobile devices and achieves 1.12s for HD (1024x768) imagery on a Windows Phone by using CPU and GPU together. The study in [26] uses DCP but substitutes guided filter with mean filter in order to increase the processing speed. It reports 25 fps over C6748 pure DSP device [27].

The study in [28] converts the hazy RGB image to HSV color space and applies a global histogram flattening on value component, modifies the saturation component to be consistent with previous reduced value and applies contrast enhancement on value component. It achieves 90ms dehazing time for HD imagery on GPU. The study in [29] conducts 2 level image processing. It first applies histogram enhancement and if the resultant image meets the system requirements then no further action is taken. If it does not, then DCP is used to remove the haze. It saves a lot of time and achieves real time processing.

[30] uses locally adaptive neighborhood and calculates order statistics. By using this information, it produces the transmission map and handles the haze-free image. The study in [31] parallelizes the base Retinex model and decompose the image into brightness and contrast components. For restoration of the image, it applies gamma correction and nonparametric mapping. It reports 1.12ms processing time for 1024x2048 high resolution image on parallel GPU system. The study in [32] constructs a transmission function estimator by using genetic programming. Then this function is used for computing the transmission map. Transmission map and hazy image are used to obtain the haze-free images. The system runs with high-rate processing time on synthetic and real-world imagery.

The literature is very rich about dehazing the single image and the video. Implementations in real time are also very interesting. However, real-time

processing is very rare on mobile devices. This study is one of the first dehazing studies on Android operating system. In this paper we follow DCP-based algorithm [18] on mobile android application.

2. MATERIALS AND METHODS

In this study we concentrate on implementing the algorithm implemented in [18] on Android operating system in real time. This method uses DCP approach, information fidelity, and image entropy to estimate atmospheric light and map transmission. The steps are prior estimation of the dark channel image, estimation of the atmospheric light, estimation of the transmission, refinement of the transmission with guided filter and reconstruction of the haze free image. Reconstruction is done using Equation 2.

The study in [18] provides very promising accuracy results. The benchmark scores for two different hazy images are given in Table 1 and 2. The images and visual results of different methods are given in Figure 3. According to Table 1 and 2, the comparisons are based on colorfulness, GCF (Global Contrast Factor) and visible edge gradient. The visible edge gradient measures the visibility using the restored and hazy images. It has three indicators e , r and σ where e is the amount of visible new edge after dehazing, r is the average ratio of gradient norm values at visible edges, and σ is the percentage of pixels after processing which becomes black or white.

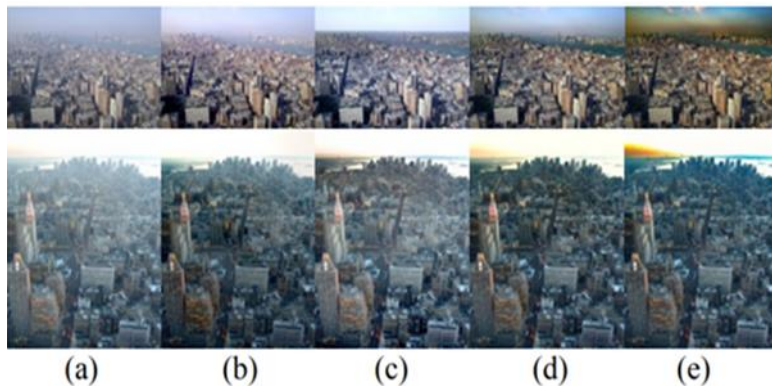


FIGURE 3. The visual comparison of several methods. (a) Hazy image (b) Study-1's result [33] (c) Study-2's result [34] (d) Study-3's result [35] (e) Result of [18].

The quality of dehazed images improves when q gets smaller and the value of other indicators increases. Although Study-1's method shows good performance in close-distance regions, it is not successful in far-range. Because it cannot remove the haze effectively. As GCF and r scores, Study-2's algorithm provides promising results, however it is not satisfactory for colorfulness and σ scores. In addition, Study-3 has limited performance, since it has good scores only for GCF and σ . The study in [18] is providing better results for overall evaluations.

TABLE 1. Accuracy results for image 1.

Index	Study-3 [35]	Study-2 [34]	Study-1 [33]	Study [18]
e	0.02	0.02	0.11	0.32
r	1.63	1.61	1.53	2.27
σ	0.01	1.35	1.7	0.06
Colorfulness	963.62	455.84	652.45	1127.42
GCF	8.63	8.53	7.87	8.49

TABLE 2. Accuracy results for image 2.

Index	Study-3 [35]	Study-2 [34]	Study-1 [33]	Study [18]
e	0.04	0.03	0.05	0.08
r	1.39	1.4	1.28	1.41
σ	0.01	0.29	9.4	0.05
Colorfulness	509.9	390.67	387.01	706.09
GCF	6.72	6.65	5.89	6.8

The main reason for choosing the study in [18] for real time implementation is its dehazing performance. Since deployment in real time is useless if we're not obtaining good results.

In the literature, as far as we are studying, there is no complete work on dehazing on the android operating system in real time. In this study, we used MATLAB SIMULINK for implementing the image dehazing technique [18]. MATLAB SIMULINK has Android device support for developing and deploying MATLAB codes and MATLAB SIMULINK models [36]. The SIMULINK model we developed is given in Figure 4.

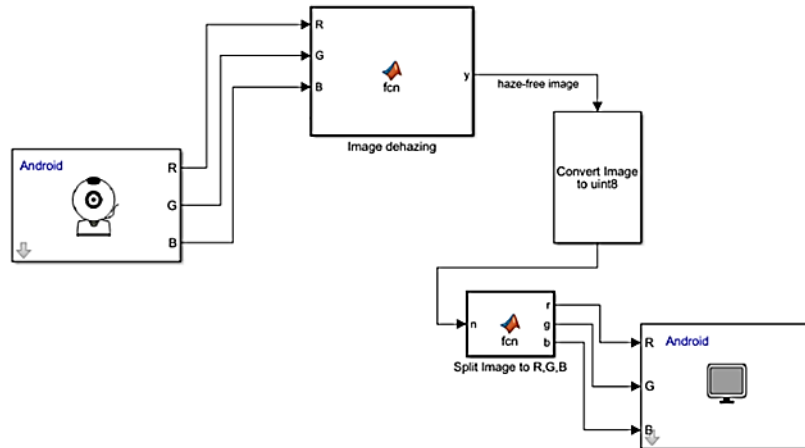


FIGURE 4. SIMULINK Model for Real-Time Implementation

The 'Android Camera' block reads live video from device's camera. The camera resolution can be set by also using this block. Real time video data is fed to the 'Image dehazing' function that runs the dehazing algorithm described in [18]. The next block in Simulink is image type conversion block which converts its input's type to double. 'Image splitting' block splits the RGB image to its color components R, G and B. Then these components are displayed on device screen by using 'Android Video Display' block.

We deployed the project on Android device by using 'Android Studio' [37]. By the way, The MATLAB codes are transferred to C++ code and a java code is produced for user updates and declare new functions. The android device we used has Qualcomm® Snapdragon™ 665 Octa-core processor, which has frequency up to 2GHz. It has 3GB RAM. The camera's video resolution is up to 4K at 30 fps.

Figure 5 shows the overall system diagram for real time implementation. Dehazing module reconstructs dehazed image by using camera data and dehazed image data is displayed on device screen.

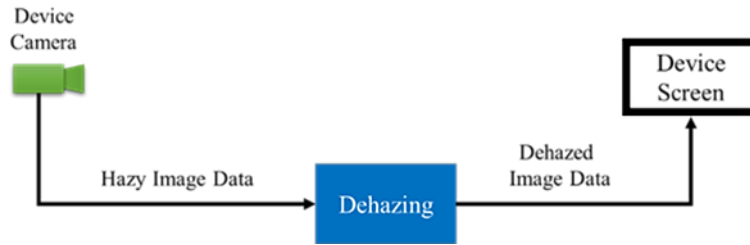


FIGURE 5. Overall System Diagram

3. RESULTS

As a real-time experimentation of the study in [18] on Android operating system, this study provides promising processing speed. The results are shown in Table 3 for different imagery resolutions.

TABLE 3. Single Image Processing Time

Resolution	Proc. Time (sec) per frame
1080p (1920x1080)	4.36
720p (1280x720)	1.95
480p (864x480)	0.87
360p (480x360)	0.36

From Table 3, we can say that the mean processing time for HD imagery is 1.95 seconds per frame. In addition, proposed approach achieves 3fps for 360p video resolution. Figure 6 shows the proposed image dehazing android application (a), hazy image (b) and dehazed image (c). Note that hazy image is displayed on a computer's screen, and the android device's camera is capturing the hazy image from computer's screen. Therefore, the dehazed image on android device's screen may be look low resolution. (despite it is high quality normally).

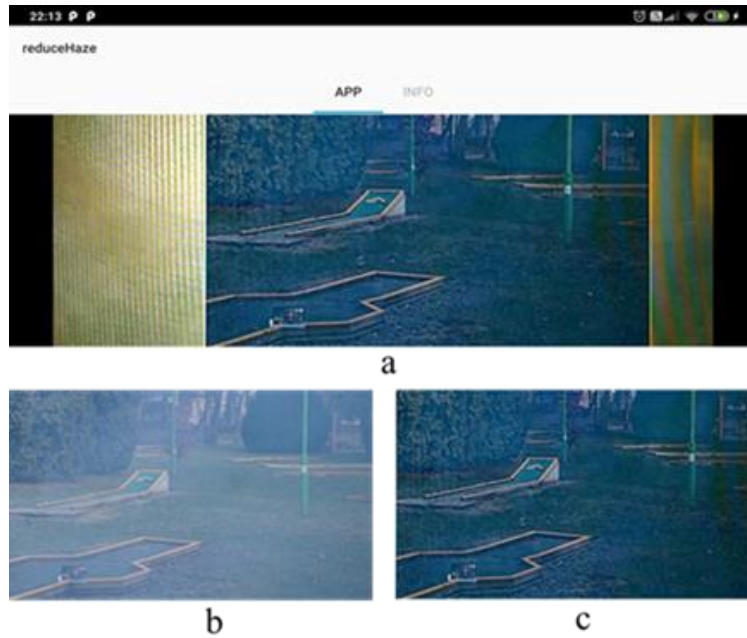


FIGURE 6. Android Dehazing Application (a) Device Screen (b) Hazy Image (c) Dehazed Image.

4. CONCLUSIONS

In this study, we implemented an image dehazing method which is described in [18] on Android operating system. The contribution of our study is implementing [18] in real time on Android operating system. We can achieve good processing time results though we use only CPU and a hardware with limited power. Processing time results show that our method can be applied in near real time on android devices. If the system is empowered in terms of hardware specifications, the processing time will decrease automatically, and the system will run in real time.

The future work should be using GPU and/or CPU and GPU together. Furthermore, similar implementation should be done on IOS devices. Another important aspect is that transmission maps may be estimated more accurately by using stereo imaging which enables estimation of depth map. Finally, image dehazing should be implemented on more powerful hardware in order to handle real time processing speed.

REFERENCES

- [1] Wang, W., Yuan, X., Recent advances in image dehazing, *IEEE/CAA Journal of Automatica Sinica*, 4(3) (2017), 410–436.
- [2] Jia, Z., Wang, H.C., Caballero, R., Xiong, Z.Y., Zhao, J.W., Finn, A., Real-time content adaptive contrast enhancement for see-through fog and rain, *Proc. IEEE Int. Conference Acoustics Speech and Signal Processing*, (2010), 1378–1381.
- [3] Al-Sammarai, M.F., Contrast enhancement of roads images with foggy scenes based on histogram equalization, *Proc. 10th International Conference on Computer Science & Education*, (2015), 95–101.
- [4] Kim, J.H., Sim, J.Y., Kim, C.S., Single image dehazing based on contrast enhancement, *Proc. IEEE International Conference Acoustics, Speech and Signal Processing*, (2011), 1273–1276.
- [5] Cai, W.T., Liu, Y.X., Li, M.C., Cheng, L., Zhang, C.X., A self-adaptive homomorphic filter method for removing thin cloud, *Proc. 19th International Conference Geoinformatics*, (2011), 1–4.
- [6] Ilgin, H., Akbulut, A., An Artifact Reduction Method For Block-Based Video Coding, *Communications Faculty of Sciences University of Ankara Series A2-A3 Physical Sciences and Engineering*, 62 (2020), 1-13.
- [7] Bülbül, A., Haj Ismail, S., Visually Enhanced Social Media Analysis Of Refugees In Turkey, *Communications Faculty of Sciences University of Ankara Series A2-A3 Physical Sciences and Engineering*, 60 (2018), 83-102.
- [8] Gibson, K.B., Belongie, S. J., Nguyen, T. Q., Example based depth from fog, *Proc. 20th IEEE International Conference on Image Processing*, (2013), 728–732.
- [9] Fang, S., Xia, X. S., Xing, H., Chen, C. W., Image dehazing using polarization effects of objects and airlight, *Opt. Express*, 22(16) (2014), 19523–19537.
- [10] Galdran, A., Vazquez-Corral, J., Pardo, D., Bertalmio, M., Enhanced variational image dehazing, *SIAM Journal of Imaging Science*, 8(3) (2015), 1519–154.
- [11] Son, J., Kwon, H., Shim, T., Kim, Y., Ahu, S., Sohng, K., Fusion method of visible and infrared images in foggy environment, *Proc. International Conference on Image Processing, Computer Vision, and Pattern Recognition*, (2015), 433–437.
- [12] Ancuti, C.O., Ancuti, C., Single image dehazing by multi-scale fusion, *IEEE Transaction on Image Processing*, 22(8) (2013), 3271–3282.
- [13] Ma, Z. L., Wen, J., Zhang, C., Liu, Q. Y., Yan, D. N., An effective fusion defogging approach for single sea fog image, *Neurocomputing*, 173 (2016), 1257–1267.
- [14] Guo, F., Tang, J., Cai, Z.X., Fusion strategy for single image dehazing, *International Journal of Digital Content Technology and Its Applications*, 7(1) (2013), 19–28.
- [15] Zhang, H., Liu, X., Huang, Z.T., Ji, Y.F., Single image dehazing based on fast wavelet transform with weighted image fusion, *Proc. IEEE International Conference on Image Processing*, (2014), 4542–4546.
- [16] Hao, W., He, M., Ge, H., Wang, C., Qing-Wei G., Retinex-Like Method for Image Enhancement in Poor Visibility Conditions, *Procedia Engineering*, 15 (2011).
- [17] Kaiming, H., Jian, S., Xiaoou, T., Single Image Haze Removal Using Dark Channel Prior, *IEEE Transactions on pattern analysis and machine intelligence*, (2011).

- [18] Park, D., Park, H., Han, D. K., Ko, H., Single image dehazing with image entropy and information fidelity, *IEEE International Conference on Image Processing (ICIP)*, (2014), 4037-4041.
- [19] Li, J., Li, G., Fan, H., Image Dehazing Using Residual-Based Deep CNN, *IEEE Access*, 6 (2018), 26831-26842.
- [20] Li, C., Guo, J., Porikli, F., Fu, H., Pang, Y., A Cascaded Convolutional Neural Network for Single Image Dehazing, *IEEE Access*, 6 (2018), 24877-24887.
- [21] Haouassi, S., Di, W., Image Dehazing Based on (CMTnet) Cascaded Multi-scale Convolutional Neural Networks and Efficient Light Estimation Algorithm, *Applied Sciences*, (2020).
- [22] Cai, B., Xu, X., Jia, K., Qing, C., Tao, D., DehazeNet: An End-to-End System for Single Image Haze Removal, *IEEE Transactions on Image Processing*, 25(11) (2016), 5187-5198.
- [23] Rashid, H., Zafar, N., Javed Iqbal, M., Dawood, H., Dawood, H., Single Image Dehazing using CNN, *Procedia Computer Science*, 147 (2019), 124-130.
- [24] Hassan, H., Bashir, A.K., Ahmad, M. et al., Real-time image dehazing by superpixels segmentation and guidance filter, *Journal of Real-Time Image Proc.*, (2020).
- [25] Yuanyuan, S., Yue. M., Single Image Dehazing on Mobile Device Based on GPU Rendering Technology, *Journal of Robotics, Networking and Artificial Life*, (2015).
- [26] Lu, J., Dong, C., DSP-based image real-time dehazing optimization for improved dark-channel prior algorithm, *Journal of Real-Time Image Processing*, (2019).
- [27] C6748 pure DSP device data sheet : Available on: https://www.ti.com/lit/ml/sprt633/sprt633.pdf?ts=1597690676332&ref_url=https%253A%252F%252Fwww.google.com%252F
- [28] Vazquez-Corral, J., Galdran, A., Cyriac, P. et al., A fast image dehazing method that does not introduce color artifacts, *Journal of Real-Time Image Processing*, 17 (2020), 607-622.
- [29] Yang, J., Jiang, B., Lv, Z. et al., A real-time image dehazing method considering dark channel and statistics features, *Journal of Real-Time Image Processing*, 13 (2017), 479-490.
- [30] Diaz-Ramirez, V.H., Hernández-Beltrán, J.E. & Juarez-Salazar, R, Real-time haze removal in monocular images using locally adaptive processing, *Journal of Real-Time Image Processing*, 16 (2019), 1959–1973.
- [31] Cheng, K., Yu, Y., Zhou, H. et al., GPU fast restoration of non-uniform illumination images, *Journal of Real-Time Image Processing*, (2020).
- [32] Hernandez-Beltran, J., Diaz-Ramirez, V., Juarez-Salazar, R., Real-time image dehazing using genetic programming, *Journal of Optics and Photonics for Information Processing*, 13, (2019).
- [33] Fattal, R., Single image dehazing, *Proc. of ACM SIGGRAPH*, 08 (2008).
- [34] Kopf, J., Neubert, B., Chen, B., Cohen, M., Cohen-Or, D., Deussen, O., Uyttendaele, M., Lischinski, D., Deep photo: Modelbased photograph enhancement and viewing, *ACM Trans. Graph.*, 27(5) (2008), 1-10.
- [35] He, K., Sun J., Tang, X., Single Image Haze Removal Using Dark Channel Prior, *IEEE Transactions on Pattern Analysis and Machine Intelligence*, 33(12) (2011), 2341-2353.

- [36] Simulink Android Support: Available on: <https://www.mathworks.com/hardware-support/android-programming-simulink.html>.
- [37] Android Studio. Available on: <https://developer.android.com/studio>.

INSTRUCTIONS TO CONTRIBUTORS

Communications Faculty of Sciences University of Ankara Series A2-A3: Physical Sciences and Engineering is a peer reviewed journal which has been published since 1948 by Ankara University, accepts original research articles written in English in the fields of Physics, Engineering Physics, Electronics/Computer Engineering, Astronomy and Geophysics. Review articles written by eminent scientists can also be invited by the Editor.

The publication costs for *Communications Faculty of Sciences University of Ankara Series A2-A3* are covered by the journal, so authors do not need to pay an article-processing and submission charges. The PDF copies of accepted papers are **free of charges** and can be downloaded from the website. Hard copies of the paper, if required, are due to be charged for the amount of which is determined by the administration each year.

Manuscripts should be typeset using a **word processor** editor. Authors should prepare the article using the COMMUNICATIONS style before **submission to the editor via our submission system**. Manuscripts written in **any plain TeX** format are also acceptable. A **template of manuscript** can be downloaded in **doc** form from the link <http://dergipark.org.tr/download/journal-file/13094> (or can be reviewed in pdf form). Authors are required to submit their Open Researcher and Contributor ID (ORCID) 's which can be obtained from <http://orcid.org> as their URL address in the format <http://orcid.org/xxxx-xxxx-xxxx-xxxx>. Acknowledgements should be given as short as possible at the end of the text. Formulas should be numbered consecutively in parentheses. The following format for the references should be used. Authors are urged to use the **Communication.csl** style (<https://dergipark.org.tr/en/download/journal-file/18514>) in **Mendeley Desktop** or **Zotero** automated bibliography. If manual entry is preferred for bibliography, then all citations must be listed in the references part and vice versa. Below, It has no relationship with the text, but can be used to show sample citations such as; for articles [1, 4], for books/booklets/theses [3], and for proceedings/conferences etc. [2].

- [1] Demirci, E., Unal, A., Özalp, N., A fractional order SEIR model with density dependent death rate, *Hacetatepe J. Math. Stat.*, 40 (2) (2011), 287–295.
- [2] Gairola, A. R., Deepmala, Mishra, L. N., Rate of approximation by finite iterates of q-Durrmeyer operators, *Proc. Natl. Acad. Sci. India Sect. A Phys. Sci.*, 86 (2) (2016), 229–234.
- [3] Lehmann, E. L., Casella, G., Theory of Point Estimation, Springer, New York, 2003.
- [4] Özalp, N., Demirci, E., A fractional order SEIR model with vertical transmission, *Math.Comput. Model.*, 54 (1-2) (2011), 1–6, <https://dx.doi.org/10.1016/j.mcm.2010.12.051>.

After the acceptance of manuscripts for publication, we will ask you to submit the TeX form of the manuscript prepared in accordance with the style of the Journal. Authors are required to submit their Open Researcher and Contributor ID (ORCID) 's which can be obtained from <http://orcid.org> as their URL address in the format <http://orcid.org/xxxx-xxxx-xxxx-xxxx>. Manuscripts should be submitted in the **PDF** form together with **THE COVER LETTER** (<http://dergipark.org.tr/download/journal-file/14088>) In the cover letter please suggest potential peer reviewers for your manuscript and please provide institutional email addresses where possible, or information which will help the Editor to verify the identity of the reviewer (for example an ORCID or Scopus ID). In the cover letter, you may enter details of anyone who you would prefer not to review your manuscript. Note that in **the cover letter**, authors should nominate **three potential reviewers** and the most appropriate **Field Editor** of the research. The editorial office may not use these nominations, but this may help to speed up the selection of appropriate reviewers.

The Editor may seek the advice of two, or three referees, depending on the response of the referees, chosen in consultation with appropriate members of the Editorial Board, from among experts in the field of specialization of the paper. The reviewing process is conducted in strict confidence and the identity of a referee is not disclosed to the authors at any point since we use a **single-blind peer review process**.

- ✓ Copyright on any open access article in *Communications Faculty of Sciences University of Ankara Series A2-A3* is licensed under a [Creative Commons Attribution 4.0 International License](https://creativecommons.org/licenses/by/4.0/) (CC BY).
- ✓ Authors grant Faculty of Sciences of Ankara University a licence to publish the article and identify itself as the original publisher.
- ✓ Authors also grant any third party the right to use the article freely as long as its integrity is maintained and its original authors, citation details and publisher are identified.

It is a fundamental condition that articles submitted to **COMMUNICATIONS** have not been previously published and will not be simultaneously submitted or published elsewhere. After the manuscript has been accepted for publication, the author will not be permitted to make any new additions to the manuscript.

Before publication the galley proof is always sent to the author for correction. Thus it is solely the author's responsibility for any typographical mistakes which occur in their article as it appears in the Journal. The contents of the manuscript published in the COMMUNICATIONS are the sole responsibility of the authors.

With the submission of the manuscript authors declare that:

- All authors of the submitted research paper have directly participated in the planning, execution, or analysis of study;
- All authors of the paper have read and approved the final version submitted;
- The contents of the manuscript have not been submitted, copyrighted or published elsewhere and the visual-graphical materials such as photograph, drawing, picture, and document within the article do not have any copyright issue;
- The contents of the manuscript will not be copyrighted, submitted, or published elsewhere, while acceptance by the Journal is under consideration.
- The article is clean in terms of plagiarism, and the legal and ethical responsibility of the article belong to the author(s). Author(s) also accept that the manuscript may go through plagiarism check using IThenticate software;
- The objectivity and transparency in research, and the principles of ethical and professional conduct have been followed. Authors have also declared that they have no potential conflict of interest (financial or non-financial), and their research does not involve any human participants and/or animals.

Research papers published in **Communications Faculty of Sciences University of Ankara** are archived in the [Library of Ankara University](https://dergipark.org.tr/) (Volume 1-60) and [Dergipark](https://dergipark.org.tr/) immediately following publication with no embargo.

Editor in Chief
Commun. Fac. Sci. Univ. Ank. Ser. A2-A3.
Ankara University, Faculty of Sciences
06100, Besevler - ANKARA TURKEY

C O M M U N I C A T I O N S

FACULTY OF SCIENCES
UNIVERSITY OF ANKARA

DE LA FACULTE DES SCIENCES
DE L'UNIVERSITE D'ANKARA

Series A2-A3: Physical Sciences and Engineering

Volume 62

Number : 2

Year :2020

L. ÖZBEK, L. SÜTÇİGİL, H. AYDIN, S. YETKİN, F. ÖZGEN, A statistical overview on sleep scoring	115
K. CENGİZ, Analyzing the performance of pure lateration in indoor environments with various performance metrics	123
A. BEKTAŞ, H. ERGEZER, LPI radar waveform classification using binary SVM and multi-class SVM based on principal components of TFI	134
M. ÜNAL, E. BOSTANCI, M.S. GUZEL, A. AYDIN, Modern learning techniques and plant image classification	153
İ. NAVRUZ, M.BİLSEL, A concatenated up and down tapered fiber for simultaneous measurement of strain and temperature..	164
Y. CİMTAY, Towards real time image dehazing on android operating system	177